Seeing around corners: Cells solve mazes and respond at a distance using attractant breakdown.

Authors: Luke Tweedy[1], Peter A. Thomason[1], Peggy I. Paschke[1], Kirsty Martin[1,2], Laura M. Machesky[1,4], Michele Zagnoni[3], Robert H. Insall[1, 4]*

Affiliations:

[1]CRUK Beatson Institute, Switchback Road, Glasgow G61 1BD, UK & [4]Institute for Cancer Sciences, University of Glasgow, G61 1QH, UK.

[2] Present address: CRUK AstraZeneca Antibody Alliance Laboratory, Granta Park, Cambridge CB21 6GS, UK.

[3]Centre for Microsystems and Photonics, Electronic and Electrical Engineering, University of Strathclyde, Glasgow, G1 1XW, UK.

*Correspondence to: Robert.Insall@glasgow.ac.uk, (44/0) 141 330 4005

Abstract:

During development and metastasis, cells migrate large distances through complex environments. Migration is often guided by chemotaxis, but simple chemoattractant gradients between a source and sink cannot direct cells over such ranges. We describe how self-generated gradients, created by cells locally degrading attractant, allow single cells to navigate long, tortuous paths and make accurate choices between live channels and dead ends. This allows cells to solve complex mazes efficiently. Cells' accuracy at finding live channels was determined by attractant diffusivity, cell speed, and path complexity. Manipulating these parameters directed cells in mathematically predictable ways; specific combinations can even actively misdirect them. We propose that the length and complexity of many long-range migratory processes, including inflammation and germ cell migration, means self-generated gradients are needed for successful navigation.

One Sentence Summary:

Cells navigate through complex environments and solve mazes by creating their own chemotactic gradients.

Main Text:

Cells migrating in embryogenesis (*1–3*), immune responses (*4*, *5*) and neural pathfinding (*6*, *7*) steer using chemotaxis, migrating up gradients of attractants such as chemokines and netrins. Simple chemotaxis, in which gradients are established between a localised attractant source and an external sink, only provides short-range guidance (*8*). It becomes inefficient at distances above 500μm (*9*), cannot resolve complex paths, and is only effective over a narrow range of attractant concentrations. These restrictions have confounded our understanding of how chemotaxis drives longer-range phenomena such as neural crest migration (*10*) and cancer metastasis (*11*). However, when cell groups locally break down an attractant found throughout the surroundings, they create their own local, dynamic gradients (*1*, *12–14*). These typically direct migration away from areas with a high density of cells, promoting metastasis (*15*). Such self-generated gradients work over arbitrarily long distances, and work equally robustly with a wide range of attractant concentrations (*16*). Here we set out to test their role in resolving complex paths, as for example a cell migrating through an embryo would follow. We found that cells using self-generated gradients could make accurate choices about paths they had not yet encountered. This enabled them to solve complex mazes, even when the initial environment was homogeneous and the correct destination was distant. Computational models, combined with live observations using microfluidic devices (*17*), reveal that the accuracy of decisions in complex environments is determined by the complexity and lengths of the paths, and the migration speeds of the cells. This mechanism explains how cells can be guided over far greater distances than can be explained by simple chemotaxis, and can interpret environmental features in a way that would be impossible with simple attractant sources.

Self-generated gradients promote long-range chemotaxis.

Chemotactic cells detect attractant gradients by comparing receptor occupancy at different places. Cells can resolve 1% differences (*18*) between the occupancy at their fronts and rears, but this is only enough to navigate short distances. Beyond 0.5-1mm, gradients contain zones that are either too shallow or too saturating to cause a 1% occupancy difference, and thus become undetectable (*9*). However, cells can make sharp, local gradients by breaking down attractants.

The resulting dynamic, self-generated gradients are usually impossible to measure directly. They are best analysed using computational models, with the predictions of the models tested experimentally in quantitative experiments on living cells. Fig. 1A & Movie S1 show modelled cells responding to a passive 1mm gradient or to a self-generated gradient in which the attractant is broken down by a cell-surface enzyme. Passive gradients of this distance are either too shallow or, if steeper, rapidly saturate the receptors; cells therefore always steer poorly in simple 1mm gradients. In contrast, the self-generated gradient gives robust chemotaxis throughout, because the gradient is always sharp and local to the group of cells that makes it, resulting a non-saturating attractant concentration around the cells (Fig. 1A & Movie S1). Secreted enzymes give similar results (*9*). Real cells behaved the way the model predicts (Fig. 1B, Movie S1).

Self-generated gradients allow cells to make long-range route decisions

Chemotaxis studies often ignore diffusion, because they consider the steady state of imposed, linear gradients (*19*, *20*). For dynamic gradients, such as self-generated gradients, diffusion is a key determinant. Interactions between the depletion of attractant by cells, the diffusion of fresh attractant towards cells, and the movement of cells in the resulting gradients can lead to counterintuitive results. We therefore modelled the way cells make decisions at junctions (Fig. 1C-E). Even in the simple case of two equivalent routes to an attractant reservoir (Fig. 1C), self-generated and static gradients elicited different behaviours. In the static gradient each cell chose a route randomly. The self-generated gradient, on the other hand, robustly directed equal numbers of cells into each branch. Stochastic variations were balanced out – branches containing more cells evolved shallower attractant gradients, so newly-arriving cells were directed into the other branch (shown quantitatively in Fig. 1F). If one of the branches was closed off from the reservoir (Fig. 1D), the number of cells entering the closed branch was small, because the first arrivals rapidly depleted the attractant and prevented further recruitment.

When the closed branch was shorter (Fig. 1E), an unexpected behaviour emerged from the models. Before the migrating cells reached the junction, they cleared the attractant from the short branch by diffusion and therefore never made the decision to enter the short branch. In

essence, the cells sensed the space ahead of themselves at a distance, making accurate predictions about the outcome of pathways they have never visited.

The effect depended strongly on the length of the dead end. Fewer than 10% of cells commited to dead ends shorter than 250µm (Fig. 1G). The time taken for attractant to diffuse out of the dead end increases quadratically with the length of the channel, so cell commitment increases dramatically with the length of the dead end. Dead ends longer than 600µm attracted 40% of exploring cells.

To investigate how cells sense closed paths without visiting them, we modelled cells following self-generated gradients through complex routes, analogous to physiological problems like finding a path from a tumour into a blood vessel. In our models, a single correct path, 1050µm long, connected each starting well to a reservoir of attractant; the number and nature of dead ends varied. Parameters were taken from measurements of *Dictyostelium* cells (*21*, *22*), which chemotax towards 3',5'- cyclic adenosine monophosphate (cAMP) while breaking it down using a cell-surface phosphodiesterase (*23*). We verified the models' predictions by fabricating identical microfluidic mazes in polydimethylsiloxane (PDMS; Fig. S2). Cells could find the correct route through all designs, despite starting with uniform chemoattractant so there were initially no directional cues. As shown below, the simulations accurately predicted the behaviour of real cells (Figs 2,3,5,6).

Self-generated gradients allow cells to navigate mazes

We found that *Dictyostelium* cells were able to navigate environments of surprising length and complexity by combining the long range of self-generated chemotaxis with the ability to detect dead ends ahead (Fig. 2). To ensure that the cells were not convolving the results by generating their own cAMP signals, we generated a new adenylyl cyclase (*aca*A) mutant in a wild-type (NC4) parent, which is healthier and migrates better than more widely used axenic strains. These cells recapitulated the models' predictions with remarkable accuracy (Movies S2-4; compare Figs 2A/B, 2D/E & 2G/H). We confirmed that the gradients were self-generated using a nondegradable ligand. Cells made almost no progress when the breakdown-resistant cAMP analogue Sp-cAMPS (*24*) was used instead of cAMP (Fig. S1, lower panels). To minimize

confounding hydraulic effects, we used 40µm x 25µm maze channels that are much wider and taller than *Dictyostelium* cells (<10µm wide and about 5µm tall).

These results show that self-generated gradients allowed cells to steer themselves through long, complex mazes that would be impossible to navigate using simple gradients.

Accuracy of decisions is controlled by length and complexity of paths

We designed three different mazes to test the accuracy of cells' decision-making strategies (Fig. 2A, D & G). Each had the same correct path, but "simple" mazes had three short, dead ends (Fig. 2A-C), "short" mazes had dead ends half the length of their live channels (Fig. 2D-F), and "long" mazes had symmetrical live and dead channels, with the only difference being the connection to the attractant reservoir (Fig. 2G-I). We tested the model's predictions using two very different cell types: *Dictyostelium* cells, and mouse pancreatic cancer cells that self-generate gradients of lysophosphatidic acid (LPA) in serum (*25*).

The model predicted that most cells avoid dead ends in the simple mazes (Fig. 2A, Movie S2). Both cell types fulfilled this prediction, with a leading group of cells migrating accurately through the maze, and a few cells deviating into the dead ends (Fig. 2B-C, Movie S3-4). Decisions were poorer in short mazes (Fig. 2D-F), and in long mazes many cells erroneously chose the dead ends (Fig. 2G-I).

To measure the dynamic fidelity of decisions, we recorded the cumulative number of cells committing to the dead ends and live channels. We observed that the error rate was highest in the first decision in each maze in both simulations and experiments, and therefore focused on the behavior at this branch point (Fig. 3A, B). The results confirmed that longer dead ends lead to poorer decision fidelity - cells performed consistently better in simple vs. long mazes, and better in general in short vs. long mazes (Fig. 3C-E; blue line shows numbers of cells choosing the correct path, and red the number committing to the dead end). Long mazes were significantly less biased over the first hour than the other designs (Fig. 3F; one-way ANOVA and Tukey's test, α=0.05).

The behaviour of cells in long mazes changed over time. Initially there was little difference between the numbers of cells choosing correctly and incorrectly, but as cells depleted the attractant in the dead ends their decisions became more accurate (Fig. 3C, D, G). The cancer cells (in homogeneous medium, where the attractant derived from the 10% serum) moved much more slowly than the *Dictyostelium* cells, but showed the same trends in decision-making (Fig. 3E, Movie S4). The similarity in behaviour between these different cell types indicates that these are general features of the chemotactic response to self-generated gradients.

Cell speed and attractant diffusivity

We supplemented our modelling and experimental approaches with a mathematical analysis that considered the effects of the lengths of the live channel and dead end on a decision at a T junction (described in detail in SI section 3.1). As real cells are not static when they decide a direction at junctions, we developed a mathematical mapping connecting the cell speed to a static waiting time; this was validated by comparing it to simulations. The analysis yielded three key predictions, shown in Fig. 4A. First, shorter dead ends gave more accurate decisions; second, shorter live ends also gave more accurate decisions; and third, decisions were more accurate if cells took longer to make them.

We had already observed the first prediction experimentally, giving confidence in the others. The second prediction resulted from two factors: for short live channels, equilibrium was quickly reached, and the resulting well-to-junction gradient was steeper. The third prediction resulted from cells having a longer time to clear attractant diffusing out of dead ends before deciding which path to take. This explains the cells' greater accuracy in the second and third decisions in the mazes (for example Fig. 3G, Movies S2-3). The same pattern was observed when cell speed in the simulations was altered, as slower cells effectively took longer to make decisions (Fig. 4B; note similarity to 4A).

These findings raised an apparent contradiction. We predicted that slower cells would make better decisions than faster ones, yet *Dictyostelium*, which solve mazes in two hours, performed similarly to cancer cells that take roughly two days. The attractants for these cells, cAMP (*26*) and LPA (*15*), have similar molecular masses, so we expected them to have similar diffusivities.

However, lipids are often carried by proteins such as albumin, slowing their effective diffusion. We predicted (Fig. 4C) the relationship between the diffusivities of cAMP and LPA that would lead to equal decision fidelity, and then performed a photobleaching assay on fluorescently labelled LPA and cAMP (Fig. 4D-E). As expected, the measured effective diffusivity of LPA was much lower than that of cAMP, and close to the value predicted by our model (10% of the cAMP value vs about 5% in our prediction, see SI Section 3.2).

This result highlights how much the accuracy of decisions in a maze depend on the rate of diffusion of the attractant. We therefore simulated the three maze designs using attractants with a range of diffusivities. The mathematical analysis predicted that high diffusivity would yield excellent decisions, and that fidelity would decrease with diffusivity to a limit where decisions were made with no information, so 50% of cells head in each direction. The models followed this prediction, with one surprising exception - cells in the short maze, but not the long maze, were predicted to do worse than 50:50 for slow-diffusing attractants with diffusivities around 1/10th that of a small molecule like LPA or cAMP (Fig. 4F-G). However, on detailed inspection, we found that in the short maze two dead-end channels were close enough to the junction to supply diffusing attractant molecules, whereas in the live channel molecules travelling a similar distance came from a single source. The quadratic relationship between diffusive flux and distance meant that branches further up the live channel had a minimal effect. This explains the behavior reversal between the short and long mazes, and again emphasizes the importance of modeling in interpreting the complex behaviors of self-generated gradients.

Complex topologies drive cells into incorrect decisions

Analysis of the counterintuitive short maze result leads to a surprising prediction – a dead end can be more attractive than a live channel, if the dead end branches or widens. This can create chemotactic mirages, which lead cells away from the source of attractant.

We built new mazes to test whether mirages actually occur. Each maze connected the cell well and large attractant reservoir with a path of identical length (around 800μm). After a variable approach, cells encountered a T junction, at which they could either migrate toward the large reservoir of attractant or down a dead end, again of variable length, towards a smaller attractant

well (Fig. 5A-C). We created and tested 16 designs in total, with four approach lengths (150, 300, 450 & 600μm) and four dead-end lengths (150,300,450 & 600μm).

We expected shorter approach lengths to yield more severe mirages for two reasons. First, a shorter approach time gives cells less time to clear attractant from the dead end. Second, the attractant well down the live path would be further away, and would therefore signal more weakly. We also predicted that short dead ends would generate stronger mirages, as a shorter distance between the side well and the junction would give a greater supply of attractant molecules from the side well. Finally, we predicted that if the live path to the large reservoir is shorter than the path to the dead end, no mirage would occur.

In simulations and experiments, short-approach, short-dead-end mazes produced a profound mirage, steering cells toward the trap (Fig. 5A, D, top panels). In intermediate designs, signals from the true reservoir were strong enough to cause some cells to reverse their initial, incorrect decision (Fig. 5 B, D, middle panels, & Movie S5). For long approaches and long dead ends, the stronger signal of the large reservoir dominates decision-making, so there is no mirage (Fig. 5C, D, bottom panels). A new prediction emerged from simulations of these designs - as these easy-to-avoid mirages move the trap a large distance away from the cell well, attractant flux through the entrance of the maze was reduced, so fewer cells were recruited (Fig. 5D- compare top and bottom panels). We measured the decision bias through the first hour for each design and found that the relationship between the lengths and decision-making holds true across all conditions and is accurately predicted by the model (Fig. 5E). The dead-end mazes confirm that most phosphodiesterase is bound to the cell surface; models where the enzyme diffuses reproduce the data much less well (Fig. S7)

These results emphasise a key result that underpins chemotaxis using self-generated gradients: the most important external determinant for decision-making is attractant flux, not attractant quantity. In the mirage maze designs, long dead ends contain more attractant than short dead ends but signal more weakly. This has obvious relevance to migration in vivo; cancer cell metastasis, for example, favours tracks with low resistance (*27*), which allow greater attractant flux.

Targeting specific outcomes in topology design.

As a final test of our models, we made two pairs of closely-related mazes. For each pair, the paths to the source and dead-end space are similar, but one was designed to be "easy" (models predict accurate decisions) and one "hard" (Movies S6-7). Easy mazes had short, weakly branched dead-ends. Hard mazes had long, highly branched dead ends, with branching beginning near the entry to maximise the mirage effect (Fig. 6).

The progress of cells was scored by counting how many passed a checkpoint after each major decision (Fig. 6A, yellow, blue & purple spots marking the checkpoints). Cell behaviour in "labyrinth" designs was strikingly similar to that predicted by the simulations (Fig. 6B & C show the first checkpoint for the easy and hard designs, respectively). Cells scored extremely divergently in the two designs, despite the similarity of the paths (Fig. 6D). A second pair, easy and hard "trident" mazes, (Fig. 6E-G) yielded very similar results (Fig. 6F-H). In both design pairs, large parts of the easy mazes were not visited, whereas the hard maze was thoroughly explored (Fig. 6I, J). Thus understanding the principles of chemotactic mazes can accurately inform how real cells respond to complex environments.

Discussion

Our results have implications for many areas of biology. We find that the detailed structure of the environments that cells encounter strikingly affects their ability to steer accurately. In many cases, self-generated gradients allow cells to steer with an accuracy that seems intuitively impossible. Changes in maze design that seem minor make a substantial – and predictable - difference to the accuracy and eventual destination of the cells. As our experimental results are accurately predicted by mathematical and computational methods, we believe that our findings are general and apply to any system in which an attractant is degraded by the cells that respond to it. This mechanism is entirely different from that used by *Physarum polycephalum* to solve mazes (*28*), which relies on the plasmodium migrating down all branches simultaneously before pruning useless paths (*29*).

Many situations where chemotaxis occurs in vivo – neutrophils extravasating to an infection in tissue (*30*), for example, or germ cells migrating through an embryo (*31*) – have equivalently complex migration paths. Similarly, attractant degradation is widespread, with examples known in immunity (*32*), development (*31*) and cancer (*33*). Chemotactic cells have a variety of mechanisms for depleting attractants, including receptor-ligand endocytosis (*34*), decoy receptors (*1*, *12*, *35*), and cell-surface enzymes that degrade attractants (*33*, *36*). Ligand breakdown is rarely considered when interpreting spatial patterns of chemotaxis data - its effects can be complex, counterintuitive and difficult to measure - but our results show it needs to be analysed and understood. Additionally, many cells create attractants as well as degrading them, and additional attractants may influence behaviour independently. The need to analyse the interactions between these complex and counterintuitive processes points to the pivotal role of computational modelling, combined with quantitative experimental measurements, in the future of biology.

We have described decisions within our mazes as correct or incorrect, but these loaded terms need not apply to in vivo contexts. Our aim is to understand how complex topology draws cells to locations that intuition would not predict. The chemotactic mirage, in which expanding and branching topologies provide more powerful chemoattraction than a direct source of chemoattractant, is particularly counter-intuitive. This could be crucial to understanding

migratory behaviour in complex in vivo environments (*11*), for example neutrophil extravasation into tissues, migration of melanoblasts through the embryonic dermis, or metastasis of glioblastoma through white matter tracts of the brain (*37*).

In summary, the interaction between the degradation of chemoattractants by cells and the structure of the landscape explains how cells navigate over long distances in complex environments. Self-generated chemoattractant gradients represent an under-studied phenomenon that could offer answers to many unexplained physiological behaviors.

Methods

Cell Lines: *aca- D. discoideum* were generated by homologous recombination in an NC4 parental background using resuspended bacteria, according to ref (*38*), and were grown non-axenically on bacterial lawns. To sensitise cells to attractant, they were collected at 1.5-3x10^7 cells/ml in development buffer (DB) and shaken for 1h, then pulsed at 6min intervals for 3.5-4h with 300nM cAMP. Cells were then pelleted and resuspended in maze medium (DB + 2.5μM cAMP + 0.05% BSA), and inoculated into the cell well at high density (~90% confluency). The cancer line used was KPC model murine pancreatic cancer (-kras -p53). Cells were cultured in DMEM+20%FCS, then trypsinised, resuspended in DMEM+10% fresh FCS and placed in the cell well of the maze. In these experiments, mazes were filled with DMEM+10% fresh FCS.

Basic chemotaxis experiments: *D. discoideum* cells were harvested, collected at 1.5-3x10^7 cells/ml in development buffer (DB) and shaken for 1.5h. Cells were then pulsed with 300nM cAMP for 4.5h at 6min intervals, bringing them into an aggregation competent state.

For fig.1 an Insall chamber was used to create a stable attractant gradient in a viewing bridge between two connected reservoirs of attractant. For an imposed gradient, the inner attractant reservoir was filled with DB containing 1μM Sp-cAMPS and the outer reservoir with attractant-free DB. For a self-generated gradient, both the inner and outer reservoir were filled with 10μM cAMP in DB. Cells were mixed into the outer well medium at a density of 2.5x10^6/ml.

Maze design and fabrication: Design schematics for mazes are given in the SI. Microfluidic mazes were fabricated in polydimethylsiloxane (PDMS; Sylgard 184, Dow Corning, US) using standard soft lithography techniques. Briefly, silicon masters were produced using SU8 3005 photoresist (3000 series, MicroChem, US) on silicon wafers following the manufacturer's protocol to achieve a final resist thickness of 25 μm. The resist was exposed through a photomask (JD Photo-Tools, UK) to collimated UV light and was developed in MicroPosit EC solvent (Rohm and Haas, US). To prevent PDMS adhesion to the silicon master, this was salinized by vapour deposition of 1H,1H,2H,2H perfluorooctyl-trichlorosilane for 1h. PDMS was poured onto the silicon master at a 10:1 ratio of base to curing agent, degassed in a vacuum desiccator chamber and cured at 70°C for at least 3 hours. PDMS devices were then peeled from

the mould, cut to the desired size and 2mm holes were punched to obtain inlet and outlet ports. PDMS devices were then cleaned and irreversibly bonded to glass-bottom petri dishes (manufacturer) using oxygen plasma.

Maze use: Mazes were filled uniformly with medium by filling all inlet ports with the medium of choice (typically ~6µl per well) and then placing into a vacuum desiccator for around 20min, degassing the PDMS. When the vacuum is released, the pressure difference draws medium into all parts of the maze, including dead ends, although this functions best if additional medium is pipetted up and down in each well, as this dislodges residual gas bubbles. Mazes used for cancer cells were pre-filled with 0.05% BSA in sterile, deionised water in order to block the PDMS and prevent any attractants from adhering. The pre-fill was dried out by first draining the wells thoroughly with a pipette, then placing in a tissue culture hood for ~2h. As soon as a maze was observed to be dry, it was re-filled with experimental medium (which, for cancer cells was Dulbecco's Modified Eagle Medium (DMEM)+10% FCS, freshly added).

Simulations: Simulations were written in Java. Diffusion in a complex environment was simulated using the semi-implicit DuFort-Frankel method. Agent-based model cells then made decisions using a persistent, biased random walk. The persistent, random element comes from drawing a new direction at each step from wrapped-normal distribution centred on the current direction of motion. The attractant gradient direction is estimated from grid points that overlap the cell (all those grid-points within 6µm of the cell centroid) and this is used to generate a bias vector. The bias vector is added to the persistent, random vector to choose a final direction of motion, and the cell moves in this direction at its current speed unless it collides with a wall- in which case, its movement distance is reduced.

Cells degrade attractant at a rate r determined by Michaelis Menten kinetics, *i.e.*

$$r = v_{max}\frac{c}{c+k_m},$$

with attractant removed evenly from all grid points overlapped by the cell.

Analysis: All decisions in mazes were binary, with cells committing to a live or a dead end. *D. discoideum* cells were counted as having committed once the whole cell body passed out of the junction into one or the other channel. Cancer cells, which are much larger, were counted as having committed once the nucleus left the junction. Decision reversals were tracked, with a cell

re-entering the junction lowering the score of its channel. In order to account for some stochastic variation from random movement, all mazes were timed from the arrival of the second cell.

All maze figures involve comparisons between designs. In all cases, these different designs were tested against one another with the same cells on the same day.

Long, short and simple mazes in Fig. 2 & 3: N=3, with 14, 14 and 12 technical replicates used for these mazes respectively.

Mirage mazes in Fig. 5: N=4, with 9-12 technical replicates performed in total for each design.

Easy and hard mazes in Fig. 6A: N=3, with 11 technical replicates of each in total.

Easy and hard mazes in Fig. 6C: N=3, with 12 technical replicates of each in total.

References and Notes:

1. E. Dona *et al.*, Directional tissue migration through a self-generated chemokine gradient. *Nature* **503**, 285 (2013).
2. M. Chuai, C. J. Weijer, Regulation of cell migration during chick gastrulation. *Current opinion in genetics & development* **19**, 343 (2009).
3. X. Yang, D. Dormann, A. E. Münsterberg, C. J. Weijer, Cell movement patterns during gastrulation in the chick are controlled by positive and negative chemotaxis mediated by FGF4 and FGF8. *Developmental cell* **3**, 425 (2002).
4. B. A. David, P. Kubes, Exploring the complex role of chemokines and chemoattractants in vivo on leukocyte dynamics. *Immunol Rev* **289**, 9 (2019).
5. I. R. Evans, W. Wood, Drosophila blood cell chemotaxis. *Curr Opin Cell Biol* **30**, 1 (2014).
6. C. E. Adler, R. D. Fetter, C. I. Bargmann, UNC-6/Netrin induces neuronal asymmetry and defines the site of axon formation. *Nat Neurosci* **9**, 511 (2006).
7. T. F. Sloan, M. A. Qasaimeh, D. Juncker, P. T. Yam, F. Charron, Integration of shallow gradients of Shh and Netrin-1 guides commissural axons. *PLoS Biol* **13**, e1002119 (2015).
8. L. Tweedy, O. Susanto, R. H. Insall, Self-generated chemotactic gradients-cells steering themselves. *Curr Opin Cell Biol* **42**, 46 (2016).
9. L. Tweedy, D. A. Knecht, G. M. Mackay, R. H. Insall, Self-Generated Chemoattractant Gradients: Attractant Depletion Extends the Range and Robustness of Chemotaxis. *PLoS Biol* **14**, e1002404 (2016).
10. R. McLennan, J. M. Teddy, J. C. Kasemeier-Kulesa, M. H. Romine, P. M. Kulesa, Vascular endothelial growth factor (VEGF) regulates cranial neural crest migration in vivo. *Dev Biol* **339**, 114 (2010).
11. E. T. Roussos, J. S. Condeelis, A. Patsialou, Chemotaxis in cancer. *Nat Rev Cancer* **11**, 573 (2011).
12. G. Venkiteswaran *et al.*, Generation and Dynamics of an Endogenous, Self-Generated Signaling Gradient across a Migrating Tissue. *Cell* **155**, 674 (2013).
13. S. R. Schwab, J. G. Cyster, Finding a way out: lymphocyte egress from lymphoid organs. *Nat Immunol* **8**, 1295 (2007).
14. C. Scherber *et al.*, Epithelial cell guidance by self-generated EGF gradients. *Integr Biol (Camb)* **4**, 259 (2012).
15. A. J. Muinonen-Martin *et al.*, Melanoma Cells Break Down LPA to Establish Local Gradients That Drive Chemotactic Dispersal. *PLoS Biol* **12**, e1001966 (2014).
16. L. Tweedy, R. H. Insall, Self-Generated Gradients Yield Exceptionally Robust Steering Cues. *Front Cell Dev Biol* **8**, 133 (2020).
17. D. Irimia, Microfluidic Technologies for Temporal Perturbations of Chemotaxis. *Annu Rev Biomed Eng* **12**, 259 (2010).
18. S. H. Zigmond, Mechanisms of sensing chemical gradients by polymorphonuclear leukocytes. *Nature* **249**, 450 (1974).
19. S. H. Zigmond, J. G. Hirsch, Leukocyte locomotion and chemotaxis. New methods for evaluation, and demonstration of a cell-derived chemotactic factor. *J Exp Med* **137**, 387 (1973).

20. D. Zicha, G. A. Dunn, A. F. Brown, A new direct-viewing chemotaxis chamber. *J Cell Sci* **99**, 769 (1991).
21. P. J. Van Haastert, Binding of cAMP and adenosine derivatives to Dictyostelium discoideum cells. Relationships of binding, chemotactic, and antagonistic activities. *J Biol Chem* **258**, 9643 (1983).
22. L. Wu, J. Franke, R. L. Blanton, G. J. Podgorski, R. H. Kessin, The phosphodiesterase secreted by prestalk cells is necessary for Dictyostelium morphogenesis. *Dev Biol* **167**, 1 (1995).
23. G. Gerisch, D. Hulser, D. Malchow, U. Wick, Cell communication by periodic cyclic-AMP pulses. *Philos Trans R Soc Lond B Biol Sci* **272**, 181 (1975).
24. C. Rossier, G. Gerisch, D. Malchow, Action of a slowly hydrolysable cyclic AMP analogue on developing cells of Dictyostelium discoideum. *J Cell Sci* **35**, 321 (1979).
25. A. Juin *et al.*, N-WASP Control of LPAR1 Trafficking Establishes Response to Self-Generated LPA Gradients to Promote Pancreatic Cancer Cell Metastasis. *Dev Cell* **51**, 431 (2019).
26. Y. Artemenko, T. J. Lampert, P. N. Devreotes, Moving towards a paradigm: common mechanisms of chemotactic signaling in Dictyostelium and mammalian leukocytes. *Cell Mol Life Sci* **71**, 3711 (2014).
27. P. G. Gritsenko, O. Ilina, P. Friedl, Interstitial guidance of cancer invasion. *The Journal of pathology* (2012).
28. T. Nakagaki, H. Yamada, A. Tóth, Maze-solving by an amoeboid organism. *Nature* **407**, 470 (2000).
29. T. Nakagaki, H. Yamada, A. Tóth, Path finding by tube morphogenesis in an amoeboid organism. *Biophys Chem* **92**, 47 (2001).
30. E. Kolaczkowska, P. Kubes, Neutrophil recruitment and function in health and inflammation. *Nature reviews immunology* **13**, 159 (2013).
31. A. D. Renault, P. S. Kunwar, R. Lehmann, Lipid phosphate phosphatase activity regulates dispersal and bilateral sorting of embryonic germ cells in Drosophila. *Development* **137**, 1815 (2010).
32. B. Breart *et al.*, Lipid phosphate phosphatase 3 enables efficient thymic egress. *J Exp Med* **208**, 1267 (2011).
33. O. Susanto *et al.*, LPP3 mediates self-generation of chemotactic LPA gradients by melanoma cells. *J Cell Sci* **130**, 3455 (2017).
34. M. A. Puthenveedu *et al.*, Sequence-dependent sorting of recycling proteins by actin-stabilized endosomal microdomains. *Cell* **143**, 761 (2010).
35. A. Rot *et al.*, Cell-autonomous regulation of neutrophil migration by the D6 chemokine decoy receptor. *J Immunol* **190**, 6450 (2013).
36. G. L. Garcia, E. C. Rericha, C. D. Heger, P. K. Goldsmith, C. A. Parent, The Group Migration of Dictyostelium Cells Is Regulated by Extracellular Chemoattractant Degradation. *Mol Biol Cell* **20**, 3295 (2009).
37. C. Denier, A. F. Carpentier, K. Mokhtari, J. Y. Delattre, Cerebral glioblastomas and systemic metastases. *Revue neurologique* **157**, 1531 (2001).
38. P. Paschke *et al.*, Rapid and efficient genetic engineering of both wild type and axenic strains of Dictyostelium discoideum. *PLoS One* **13**, e0196809 (2018).

Acknowledgments:

We are very grateful to Dr. Rebecca Ward for several rounds of helpful comments on the manuscript and presentation, Dr. Heather Spence for assistance with tissue culture, and to the members of Beatson Advanced Imaging Resource (BAIR) for help with microscopy.

Funding:

Funded by core grants (A24450 & A15673) to RI & LM, a multidisciplinary project award (A20017) from Cancer Research UK to RI, CRUK Beatson Institute Core Services and Advanced Technologies (C596/A17196), and internal Strathclyde University Funds to MZ.

Author contributions:

LT: Conceptualization, Formal analysis, Investigation, Software, Visualization, Writing – original draft

PT: Investigation, Writing – review & editing

PP: Methodology

KM: Methodology

LM: Conceptualization, Writing – review & editing

MZ: Methodology, Funding acquisition

RI: Conceptualization, Funding acquisition , Supervision, Visualization

Competing interests:

MZ is co-founder and CSO of ScreenIn3D Limited. Authors declare no other competing interests.

Code availability:

Source code is available on github at https://github.com/ltweedy/MazeNavigation.

Fig. 1: Self generated gradients allow cells to explore remote features.

(A) Comparison of imposed and self-generated gradients guiding cells across 1mm to a full attractant well. **(B)** Experimental verification of (A) using *Dictyostelium discoideum*. The imposed gradient uses the non-degradable attractant Sp-cAMPS. The self-generated gradient uses uniform cAMP. Cells following the imposed gradient perform worse, especially after the halfway point. Bar 50μm. See Movie S1.

(C-E) Simulated navigation past a junction. In (C) both branches are identical and connect to an attractant reservoir. Each recruits the same number of cells. In (D) one branch is a dead end. Some cells do still commit due to residual attractant in the channel. In (E), the dead end is much shorter, and is almost entirely free of attractant as the cells reach the junction. **(F)** Number of cells selecting the top channel through repeated simulations of (C). Concentration is tuned so an average of 24 cells commit. The self-generated gradient has a smaller standard deviation than a random choice, revealing active sorting. **(G)** The fraction of cells committing to a dead end as a function of its length. Few cells commit to short dead ends, but there is an apparently linear increase from 250μm-650μm. Above this, the fraction plateaus at about 0.4.

Fig. 2: Real cells can solve mazes.

(A) Simulation of cells navigating the maze with short dead ends, at time-points past the first, second and third decisions. In this design, cells are predicted to almost always commit to the correct path to lead them to the attractant well. **(B)** *Dictyostelium* cells migrating through the same maze design, initially filled uniformly with the attractant cAMP. **(C)** Pancreatic cancer cells in the same maze design, with an initial background of 10% FCS. **(D-F)** Simulations of the short-branched maze (D), compared with *Dictyostelium* (E) and pancreatic cancer (F) cells navigating the same design. **(G-I)** Simulations of the long-branched maze design (G), compared with *Dictyostelium* (H) and pancreatic cancer (I) cells. See Movies S2 (A,D,G) , S3 (B,E,H) & S4 (C,F,I). Device width 850µm; channel width 40µm; channel height 25µm.

Fig. 3: More distant and complex dead ends are harder to resolve.

(A) Simulations of the long-, short-, and simple-branched mazes as the cells reach the junction between the live path and the first dead end. **(B)** The same simulations at a later time. Cell colour has been altered for those that have committed to the live end (deep blue) or dead end (red). Uncommitted cells are shown in the original grey blue. **(C-E)** Running totals of cells committed to the live end (blue) and dead end (red), as pictured in (B). Results are shown for simulations (C), *Dictyostelium* (D) and pancreatic cancer experiments (E), with t=0 when cells first reach the entrance to the maze. Light blue shading highlights the difference between these values. **(F)** Decision fidelity scores for *Dictyostelium* cells at the first junction of each maze. The simple- and short-branched mazes both differ significantly in their fidelity to the long-branched maze (one-way ANOVA, α=0.05). **(G)** Overall decision fidelity scores for the simulations compared with their experimental counterparts. Decision fidelity is $\langle t - f \rangle / \langle t + f \rangle$ over a 1hr window, where t and f are the number currently committed to the correct and incorrect paths. Later decisions generally have higher fidelity.

Fig. 4: Slower cells and faster diffusion lead to more accurate decisions.

(A) Mathematical model of decision fidelity at a T junction. Each panel shows a snapshot after a different waiting time at the junction before making decision. Lengths of the live and dead ends on x and y axes, respectively. **(B)** Decisions made by simulated cells moving at different speeds, and therefore taking different times to reach the junction so as to correspond with the panels above. **(C)** To correct for cell movement sharpening the gradient, we create a mapping from the solvable static model to an adjusted model. The static and adjusted models are shown for three cell speeds against the true gradient seen in the simulations. **(D)** Photobleaching of 8-fluo-cAMP and TopFluor Lyso PA. **(E)** Recovery curves & fits for the photobleached areas suggest that the effective diffusivity of LPA is ~$1/10^{th}$ that of cAMP. Bar 50µm. **(F)** Expected decision fidelities for the short-branched maze across time, simulated over a variety of attractant diffusivities. Notably, a phase change in behaviour occurs for lower diffusivities, in which a majority of cells choose the dead end. This does not happen in the long-branched maze, revealing that, in branching topologies, shorter dead ends may in fact lead to worse decisions. **(G)** Snapshots of three simulations at the three numbered points in (F).

Fig. 5: Cell decisions depend on the rate of attractant transport.

(A-C) Using 4 dead-end lengths and 4 junction approach lengths (labelled in (B)), we generate 16 mazes in total with varying predictions of cell behaviour. We show real cells (left) and simulation predictions (right) for 3 of the 16 designs. (A) shows short approach length and dead-end length (both 150µm). (B) shows a 150µm dead end and a 450µm approach, with cells faring better than in (A). (C) shows an approach length and a dead-end length of 600µm. In this case, cells overwhelmingly steer correctly toward the large reservoir. Dynamics of (A-C) can be seen in Movie S5. Distance between reservoirs 800µm. **(D)** Total number of cells committing to the live- and dead-ends on average for the designs shown in A-C. Blue filling shows a positive bias (favouring the live end), while red filling shows a negative bias (favouring the dead-end). For a short approach and a short dead end, real cells have a strongly negative bias which is not

overcome within the hour-long observation (top-left). This was predicted by simulation (top-right). An intermediate approach-length and a short dead end causes a brief chemotactic mirage, but the dead-end is short enough that the misdirected cells then receive attractant flux from the large reservoir and rectify their mistake (middle left). This again is predicted (middle-right). A long approach and long dead-end (bottom-left) has two features. Firstly, the bias is consistently positive and no mirage forms. Secondly, this design recruits fewer cells overall. Both features were predicted by the simulations. (**E**) Average bias score over a 45min observation for all 16 designs. The general trend of short approach and dead ends both causing negative bias, predicted by the model (right), is seen clearly in the experimental data (left).

Fig. 6: Deliberate misdirection of live cells.

(**A)** Designs for easy and hard labyrinth mazes. Though both have the sa me amount of dead-end space, the hard labyrinth is designed with fewer, longer, and more branched dead ends. We note that the easy labyrinth is harder to solve visually. Checkpoints are marked (coloured dots). These are used to score the navigational success of cells. Devices 800µm wide. (**B-C**) Example images of cells passing the first checkpoint in both labyrinths, alongside the behaviour predicted by simulations. See Movie S6. **(D)** Number of *Dictyostelium* cells passing each checkpoint in (A) as a fraction of maze entrants. The checkpoint colour tag is shown above each value. (**E**) Designs for easy (left) and hard (right) trident mazes along similar principles to (A). Devices 810µm wide. (**F-H**) Similar images of cells navigating trident designs. See Movie S7. Pairwise *t*-testing the final decision yields $p<0.05$ for both design pairs. **(I-J)** Cell images taken at 5min intervals are colour-coded by time and superimposed on the unmoving, median image of the mazes for all four designs, showing the path taken by cells.

–

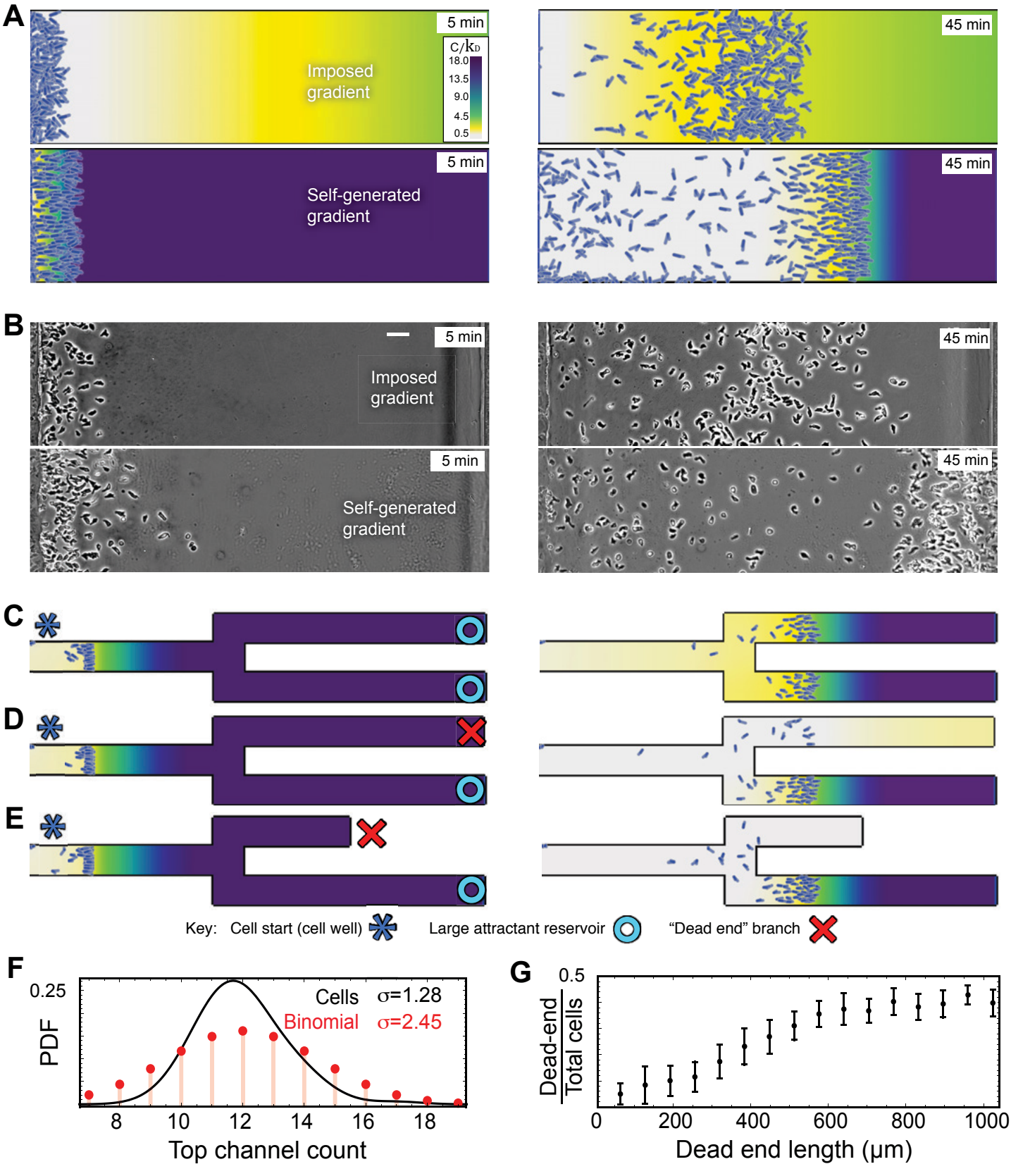
A
5 min
Imposed gradient
C/kD
18.0
13.5
9.0
4.5
0.5
5 min
Self-generated gradient
45 min
45 min
B
5 min
Imposed gradient
5 min
Self-generated gradient
45 min
45 min
C
D
E
Key: Cell start (cell well)
Large attractant reservoir
"Dead end" branch
F
0.25
PDF
Cells σ=1.28
Binomial σ=2.45
8
10
12
14
16
18
Top channel count
G
0.5
Dead-end / Total cells
0
200
400
600
800
1000
Dead end length (μm)

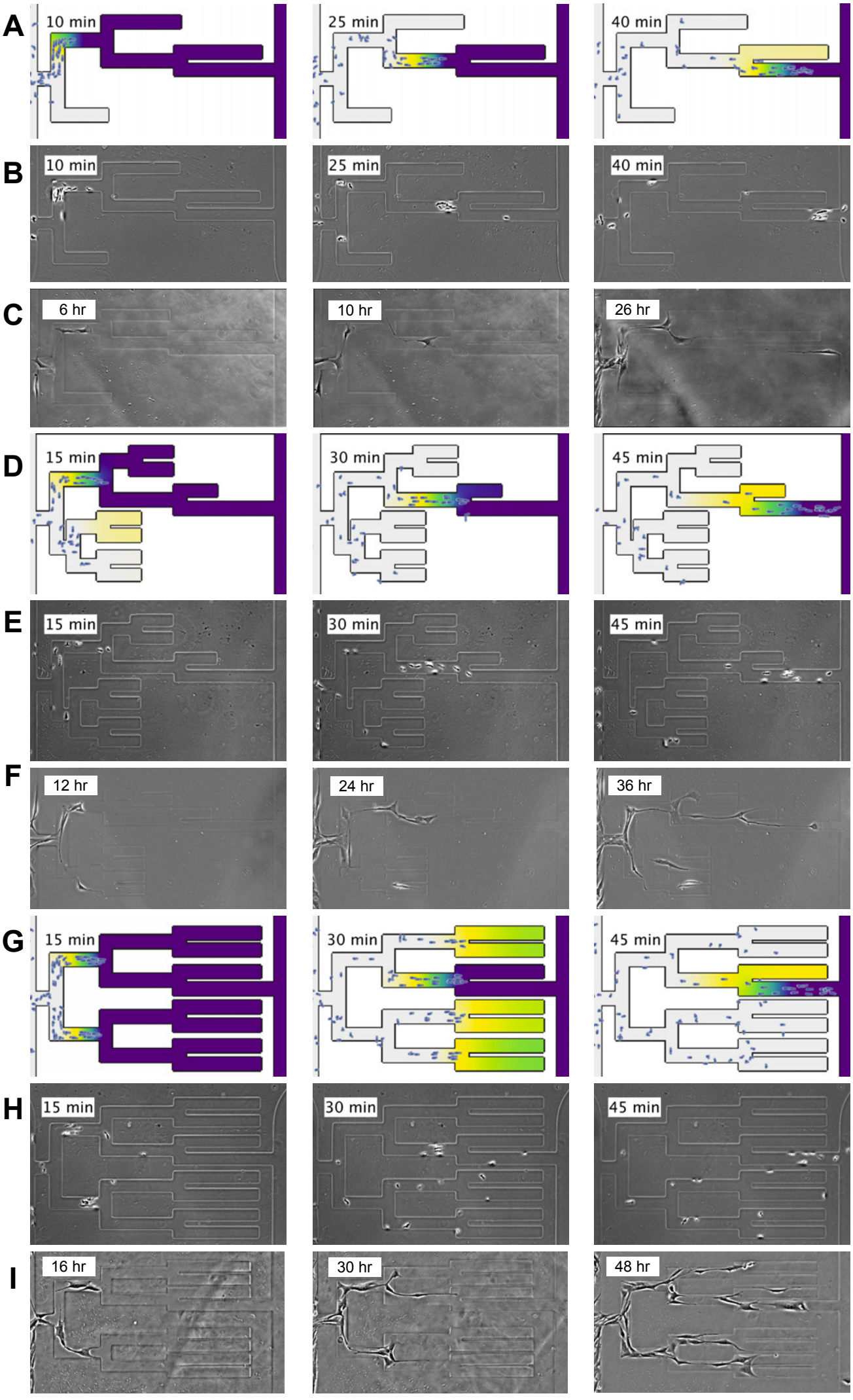
A
10 min
25 min
40 min
B
10 min
25 min
40 min
C
6 hr
10 hr
26 hr
D
15 min
30 min
45 min
E
15 min
30 min
45 min
F
12 hr
24 hr
36 hr
G
15 min
30 min
45 min
H
15 min
30 min
45 min
I
16 hr
30 hr
48 hr

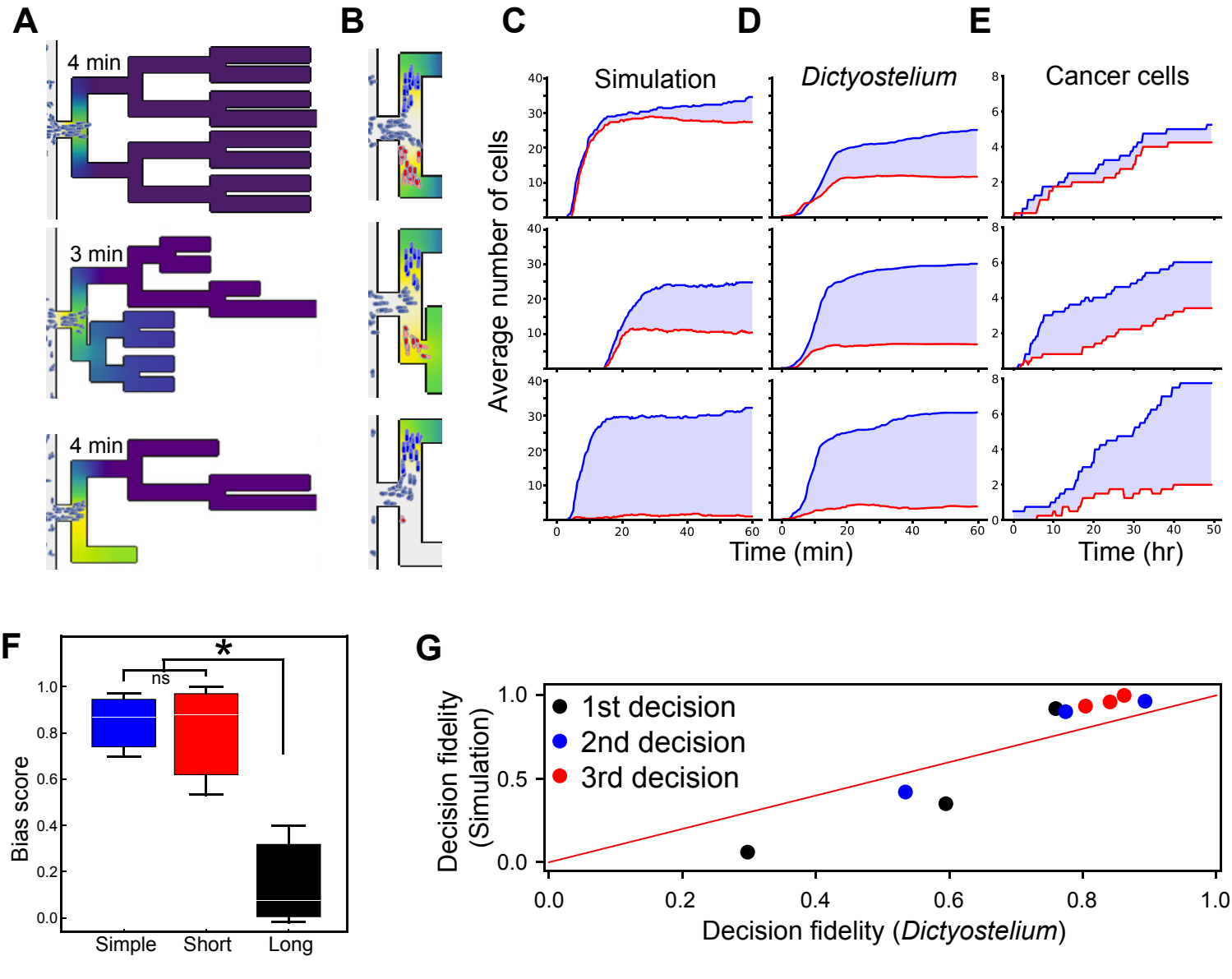
A
B
C
D
E
4 min
3 min
4 min
Simulation
Dictyostelium
Cancer cells
Average number of cells
Time (min)
Time (hr)
F
G
*
ns
Bias score
Simple
Short
Long
1st decision
2nd decision
3rd decision
Decision fidelity (Simulation)
Decision fidelity (Dictyostelium)

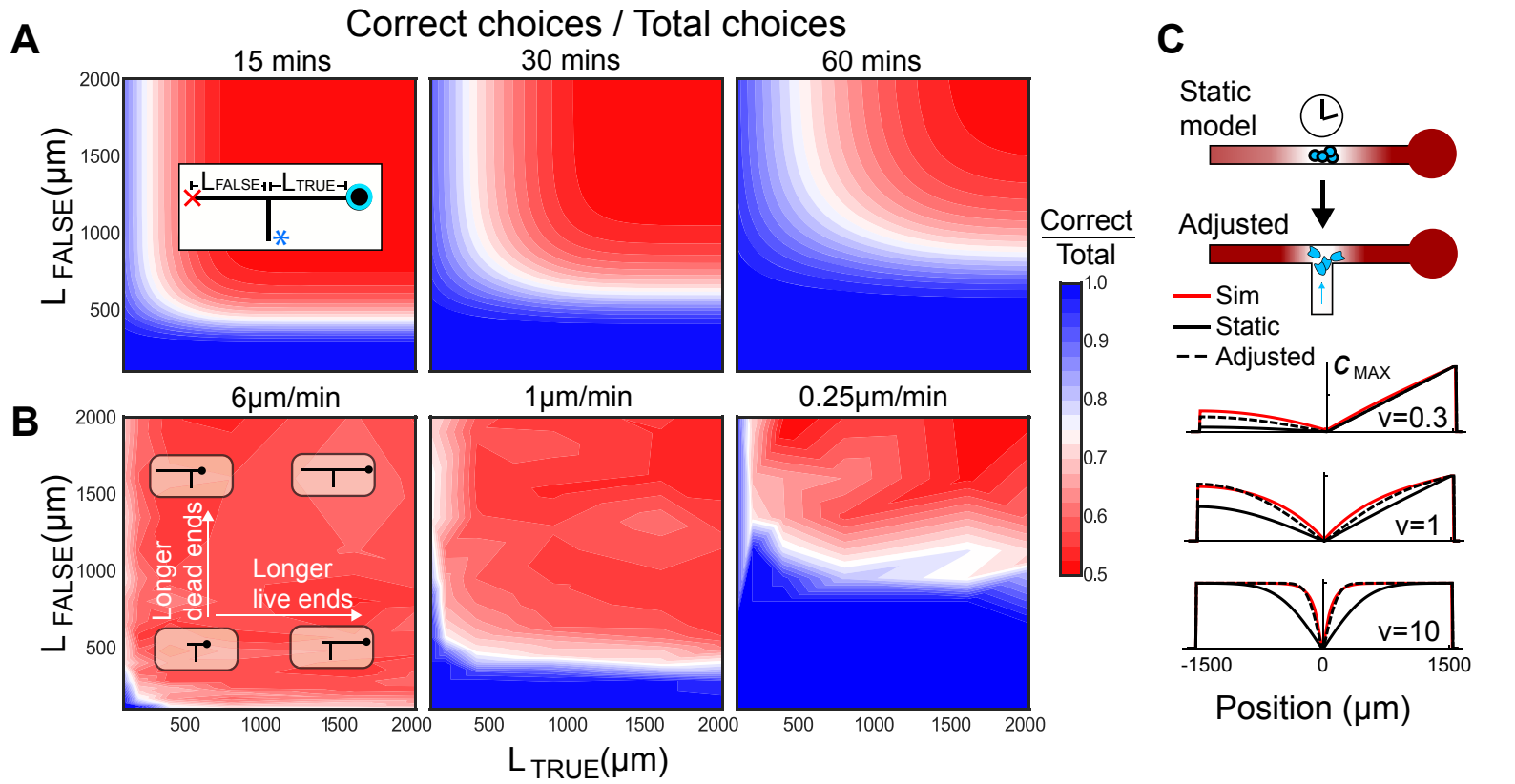
A
Correct choices / Total choices
15 mins
30 mins
60 mins
L FALSE(μm)
2000
1500
1000
500
L FALSE
L TRUE
B
6μm/min
1μm/min
0.25μm/min
Longer dead ends
Longer live ends
L TRUE(μm)
Correct / Total
1.0
0.9
0.8
0.7
0.6
0.5
C
Static model
Adjusted
Sim
Static
Adjusted
c MAX
v=0.3
v=1
v=10
-1500
0
1500
Position (μm)

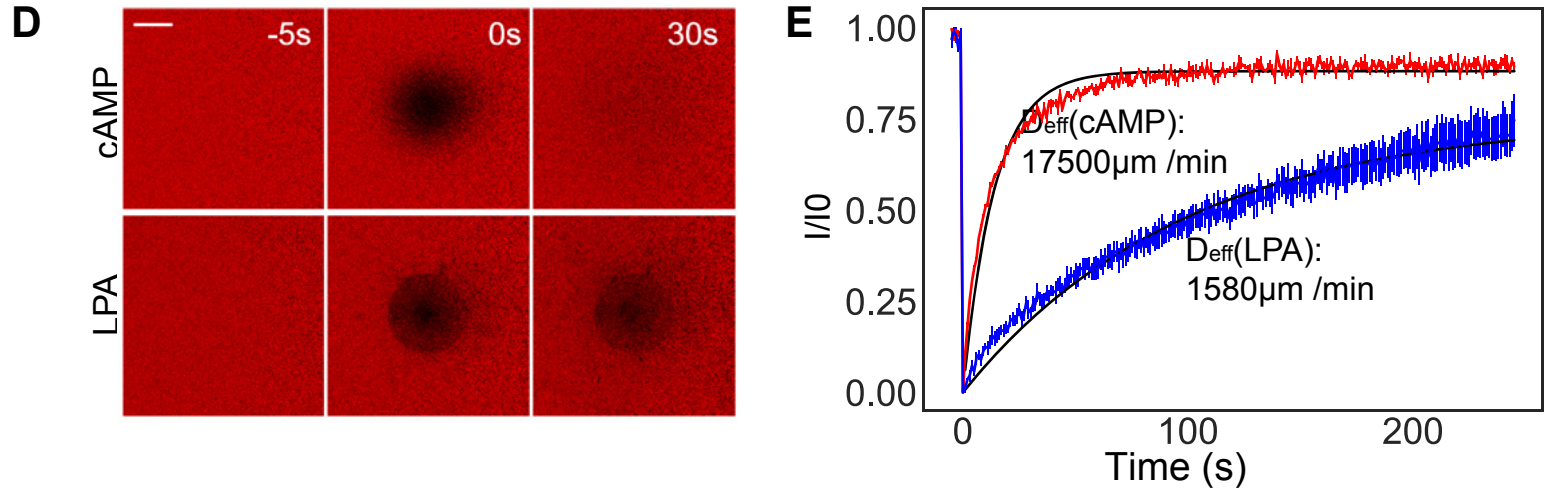
D
-5s
0s
30s
cAMP
LPA
E
I/I0
1.00
0.75
0.50
0.25
0.00
Deff(cAMP):
17500μm /min
Deff(LPA):
1580μm /min
0
100
200
Time (s)

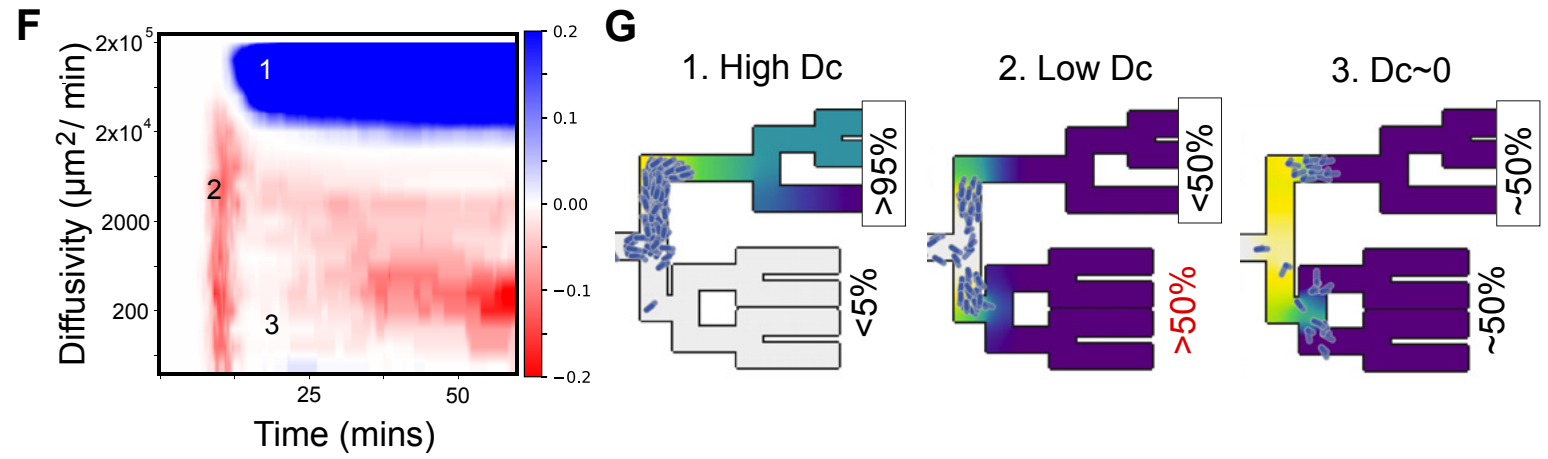
F
Diffusivity (μm2/ min)
2x10^5
2x10^4
2000
200
1
2
3
25
50
Time (mins)
0.2
0.1
0.00
−0.1
−0.2
G
1. High Dc
2. Low Dc
3. Dc~0
>95%
<5%
<50%
>50%
~50%
~50%

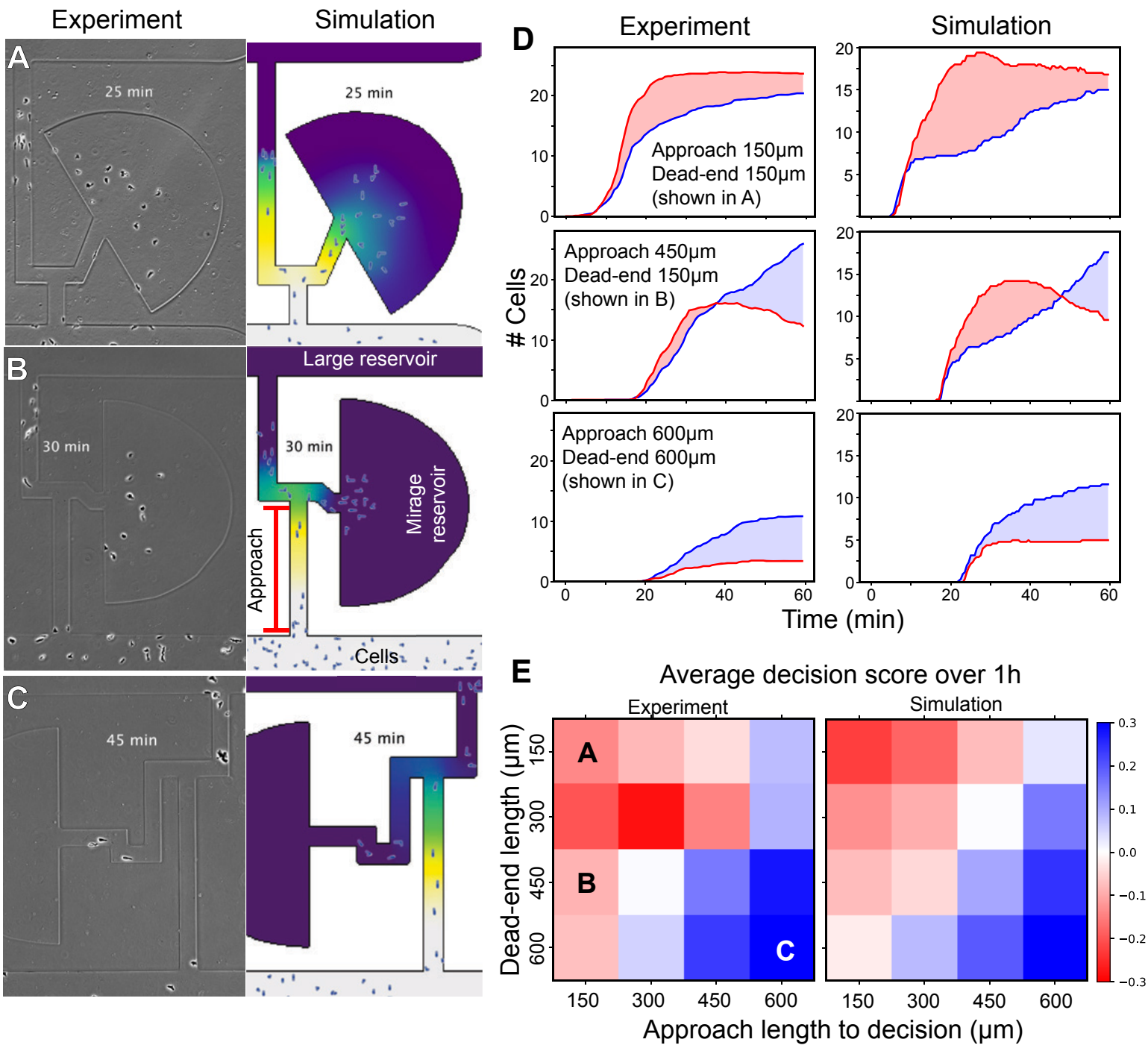
Experiment
Simulation
A
25 min
25 min
B
30 min
Large reservoir
30 min
Mirage reservoir
Approach
Cells
C
45 min
45 min
D
Experiment
Simulation
Approach 150µm
Dead-end 150µm
(shown in A)
Approach 450µm
Dead-end 150µm
(shown in B)
Approach 600µm
Dead-end 600µm
(shown in C)
Cells
Time (min)
E
Average decision score over 1h
Experiment
Simulation
Dead-end length (µm)
Approach length to decision (µm)

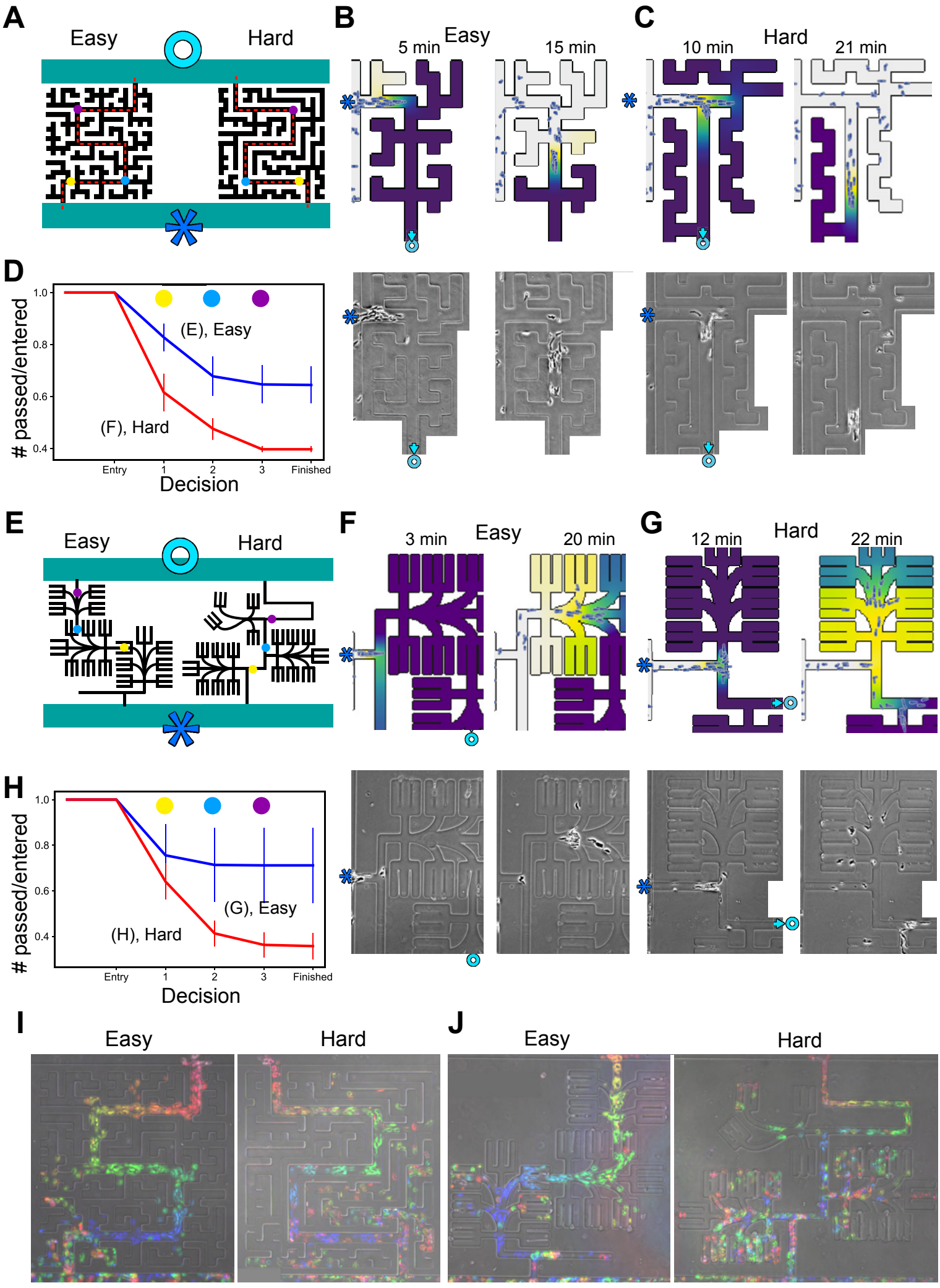
A
Easy
Hard
B
Easy
5 min
15 min
C
Hard
10 min
21 min
D
passed/entered
1.0
0.8
0.6
0.4
(E), Easy
(F), Hard
Entry
1
2
3
Finished
Decision
E
Easy
Hard
F
Easy
3 min
20 min
G
Hard
12 min
22 min
H
passed/entered
1.0
0.8
0.6
0.4
(G), Easy
(H), Hard
Entry
1
2
3
Finished
Decision
I
Easy
Hard
J
Easy
Hard

Materials and Methods

Cell Lines

aca- *D. discoideum* were generated by homologous recombination in an NC4 parental background using resuspended bacteria, according to ref (38), and were grown non-axenically on bacterial lawns. To sensitise cells to attractant, they were collected at $1.5 - 3x10^7$ cells/ml in development buffer (DB) and shaken for 1h, then pulsed at 6min intervals for 3.5-4h with 300nM cAMP. Cells were then pelleted and resuspended in maze medium (DB + 2.5μM cAMP + 0.05% BSA), and inoculated into the cell well at high density (90% confluency). The cancer line used was KPC model murine pancreatic cancer (-kras -p53). Cells were cultured in DMEM+20%FCS, then trypsinised, resuspended in DMEM+10% fresh FCS and placed in the cell well of the maze. In these experiments, mazes were filled with DMEM+10% fresh FCS.

Basic chemotaxis experiments

D. discoideum cells were harvested, collected at $1.5 - 3x10^7$ cells/ml in development buffer (DB) and shaken for 1.5h. Cells were then pulsed with 300nM cAMP for 4.5h at 6min intervals, bringing them into an aggregation competent state. For Fig.1 an Insall chamber was used to create a stable attractant gradient in a viewing bridge between two connected reservoirs of attractant. For an imposed gradient, the inner attractant reservoir was filled with DB containing 1μM Sp-cAMPS and the outer reservoir with attractant-free DB. For a self-generated gradient, both the inner and outer reservoir were filled with 10μM cAMP in DB. Cells were mixed into the outer well medium at a density of $2.5x10^6$/ml.

Maze design and fabrication

Design schematics for mazes are given in the SI. Microfluidic mazes were fabricated in polydimethylsiloxane (PDMS; Sylgard 184, Dow Corning, US) using standard soft lithography techniques. Briefly, silicon masters were produced using SU8 3005 photoresist (3000 series, MicroChem, US) on silicon wafers following the manufacturer's protocol to achieve a final resist thickness of 25 μm. The resist was exposed through a photomask (JD Photo-Tools, UK) to collimated UV light and was developed in MicroPosit EC solvent (Rohm and Haas, US). To prevent PDMS adhesion to the silicon master, this was salinized by vapour deposition of 1H,1H,2H,2H perfluorooctyl-trichlorosilane for 1h. PDMS was poured onto the silicon master at a 10:1 ratio of base to curing agent, degassed in a vacuum desiccator chamber and cured at 70° C for at least 3 hours. PDMS devices were then peeled from the mould, cut to the desired size and 2mm holes were punched to obtain inlet and outlet ports. PDMS devices were then cleaned and irreversibly bonded to glass-bottom petri dishes (manufacturer) using oxygen plasma.

Maze use

Mazes were filled uniformly with medium by filling all inlet ports with the medium of choice (typically 6μl per well) and then placing into a vacuum desiccator for around 20min, degassing the PDMS. When the vacuum is released, the pressure difference draws medium into all parts of the maze, including dead ends, although this functions best if additional medium is pipetted up and down in each well, as this dislodges residual gas bubbles. Mazes used for cancer cells were

pre-filled with 0.05% BSA in sterile, deionised water in order to block the PDMS and prevent any attractants from adhering. The pre-fill was dried out by first draining the wells thoroughly with a pipette, then placing in a tissue culture hood for 2h. As soon as a maze was observed to be dry, it was re-filled with experimental medium (which, for cancer cells was Dulbecco's Modified Eagle Medium (DMEM)+10% FCS, freshly added).

Simulations

Simulations were written in Java. Diffusion in a complex environment was simulated using the semi-implicit DuFort-Frankel method. Agent-based model cells then made decisions using a persistent, biased random walk. The persistent, random element comes from drawing a new direction at each step from wrapped-normal distribution centred on the current direction of motion. The attractant gradient direction is estimated from grid points that overlap the cell (all those grid-points within 6μm of the cell centroid) and this is used to generate a bias vector. The bias vector is added to the persistent, random vector to choose a final direction of motion, and the cell moves in this direction at its current speed unless it collides with a wall- in which case, its movement distance is reduced. Cells degrade attractant at a rate r determined by Michaelis Menten kinetics, i.e. , with attractant removed evenly from all grid points overlapped by the cell.

Analysis

All decisions in mazes were binary, with cells committing to a live or a dead end. D. discoideum cells were counted as having committed once the whole cell body passed out of the junction into one or the other channel. Cancer cells, which are much larger, were counted as having committed once the nucleus left the junction. Decision reversals were tracked, with a cell re-entering the junction lowering the score of its channel. In order to account for some stochastic variation from random movement, all mazes were timed from the arrival of the second cell. All maze figures involve comparisons between designs. In all cases, these different designs were tested against one another with the same cells on the same day. Long, short and simple mazes in Fig. 2 and 3: N=3, with 14, 14 and 12 technical replicates used for these mazes respectively. Mirage mazes in Fig. 5: N=4, with 9-12 technical replicates performed in total for each design. Easy and hard mazes in Fig. 6A: N=3, with 11 technical replicates of each in total. Easy and hard mazes in Fig. 6C: N=3, with 12 technical replicates of each in total.

1 Supplementary text

1.1 Analytical solutions for live and dead ends of a single-choice maze

Consider a maze design that presents cells with a single binary decision. They enter a channel of length L_0 from the cell well. At the far end of this channel they reach a junction. To one side, at the end of a channel of length L_T, is the attractant well. To the other, at the end of a channel of length L_F, is a dead end.

If we imagine the cells reaching this junction very rapidly, then sitting still and pondering their decision for some time t, we can describe the state of the maze piecewise, with the concentration profiles of the true and false branches $c_T(x,t), c_F(x,t)$ evolving according to the heat equation,

$$\partial_t c(x,t) = D_c \partial_{xx} c(x,t), \tag{1}$$

where D_c is the diffusivity of the attractant. Taking the decision point to be the origin for each branch, the boundary conditions for the true and false branches are:

A) $c_T(0,t) = 0, \quad c_T(L_T,t) = c_0, \quad c_T(x,0) = c_0$

B) $c_F(0,t) = 0, \quad \partial_x c_F(L_F,t) = 0, \; c_F(x,0) = c_0$

The solution method for these conditions is well known, but briefly we use variable separation to find the Fourier series solution. In both cases we can apply the first boundary condition to restrict ourselves to the Fourier sine series. In order not to violate the boundary conditions, the true branch must also include the steady state solution of a linear gradient. At this stage, we have:

$$c_T(x,t) = \frac{c_0 x}{L_T} + \sum_{n=1}^{\infty} B_n \sin\frac{n\pi x}{L_T} \exp\big(-n^2\pi^2 D_c t/L_T^2\big), \tag{2}$$

$$c_F(x,t) = \sum_{n=0}^{\infty} B_n \sin\frac{(n+\frac{1}{2})\pi x}{L_F} \exp\big(-(n+1/2)^2\pi^2 D_c t/L_F^2\big), \tag{3}$$

where in each case the B_n can be found by Fourier transformation of the initial conditions. This gives us the complete forms of $c_T(x,t)$, $c_F(x,t)$:

$$c_T(x,t) = \frac{c_0 x}{L_T} + \sum_{n=1}^{\infty} \frac{2c_0}{n\pi} \sin\frac{n\pi x}{L_T} \exp\big(-n^2\pi^2 D_c t/L_T^2\big), \tag{4}$$

$$c_F(x,t) = \frac{4c_0}{\pi} \sum_{n=0}^{\infty} \frac{1}{2n+1} \sin\frac{(n+\frac{1}{2})\pi x}{L_F} \exp\big(-(n+1/2)^2\pi^2 D_c t/L_F^2\big). \tag{5}$$

We assess the desision fidelity by taking the ratio of the number of cells committing to the true branch and the number of cells committing to the false branch. We can reasonably assume that the number of cells recruited to each branch is proportional to the attractant gradient of that branch at x=0:

$$\partial_x c_T(0,t) = \frac{c_0}{L_T}\left(1 + 2\sum_{n=0}^{\infty}\exp\big(-n^2\pi^2 D_c t/L_T^2\big)\right), \tag{6}$$

$$\partial_x c_F(0,t) = \frac{2c_0}{L_F}\sum_{n=0}^{\infty}\exp\big(-(n+1/2)^2\pi^2 D_c t/L_F^2\big) \tag{7}$$

This dependency is not due to chemotactic biases: if each cell were to sense both branches, we would expect them to commit exclusively to the steeper option. It is rather that, at the point of decision, a new self-generated gradient begins in each direction. It is because that attractant flux at $x = 0$ is linearly proportional to the gradient (by Fick's first law), and that, as we have previously reported, the number of cells recruited in a self-generated gradient is the number of cells required to break down all incoming attractant.

A rather simple review of the decision of Eqns. 6-7 shows that cells will make better decisions the longer they wait at the decision point. Comparing the ratio of the two will always show an increasing decision fidelity over time, and in the limit, as $t \to \infty$, the stationary state of the true branch is a static gradient, where the stationary state of the false branch is zero everywhere. We use these results to further explore the expected decision fidelity for any value of L_T and L_F over time in the main text.

1.2 Diffusivity of cAMP and LPA

In spite of *Dictyostelium* taking two hours to navigate a maze and KPC cancer cells taking two days, their decisions are strikingly similar. How, then, does this suggest that the other system dynamics have changed?

If we assume that decisions are made in proportional to attractant flux, we can describe this similarity by equating the ratios of Eqn. 6 to Eqn. 7 for their respective parameters:

$$\begin{aligned} f(t) &= c_T(t)/c_F(t), \\ &= \frac{L_F}{2L_T}\,\frac{1 + 2\sum_{n=1}^{\infty}\exp\big(-n^2\pi^2 D_c t/L_T^2\big)}{\sum_{m=1}^{\infty}\exp\big(-(m-1/2)^2\pi^2 D_c t/L_F^2\big)}. \end{aligned} \tag{8}$$

As the maze design parameters L_T and L_F are invariant here, this implies that $D_{c1}t_1 = D_{c2}t_2$, and, as each has to migrate the same distance in order to reach the junction, that

$$\frac{D_{c1}}{D_{c2}} = \frac{v_1}{v_2} \tag{9}$$

and that, as the speed of *Dictyostelium* migration is about 12μm/min compared with a KPC cell speed of around 0.6μm/min, the diffusivity of cAMP is correspondingly 20 times that of LPA.

1.3 Effective time approximation for the effect of cell migration on gradient steepness

A major assumption in the previous section is that the attractant profiles evolve from their initial state entirely after the cells reach the decision point. In reality, the attractant profile evolves prior to their arrival at the decision point, and the cells respond very rapidly to the current state of the maze as they reach it. We therefore need to find a way of estimating the correct value of t to use in predicting the state of the maze when the cells arrive at the decision point. The simplest choice would be to assume that the actual time taken between entering the maze and reaching the decision point t_T can be used in place of t, however we intuitively expect that our attractant-degraing cells sharpen the gradient as they migrate up it. Can we demonstrate that this is the case? And if so, can we determine an effective time to use in the stationary solution as a function of the actual length of time that has passed?

Consider a concentration profile $c(x,t)$ initially of a uniform concentration c_0 for all $x > 0$, and with the boundary conditions $c(0,t) = 0$, $c(x,t) \underset{x\to\infty}{=} c_0$. We can satisfy these conditions with the self-similar solution to the heat equation:

$$c(x,t) = c_0 \operatorname{erf} \frac{x}{\sqrt{4D_c t}}, \tag{10}$$

$$\partial_t c(x,t) = -\frac{c_0 x}{\sqrt{4\pi D_c t^3}} \exp \frac{-x^2}{4D_c t}, \tag{11}$$

$$\partial_x c(x,t) = \frac{c_0}{\sqrt{\pi D_c t}} \exp \frac{-x^2}{4D_c t}, \tag{12}$$

$$\partial_{xx} c(x,t) = -\frac{c_0 x}{\sqrt{4\pi D_c^3 t^3}} \exp \frac{-x^2}{4D_c t} \tag{13}$$

Where the factor c_0 has been chosen to satisfy the initial and boundary conditions, remembering that $\operatorname{erf} x \to 1$ as $x \to \infty$. In this case, the perfect sink is stationary at $x = 0$. We must now find a solution for a comparible situation, but where the boundary is able to move over time. We will denote the position of this moving boundary with $s(t)$, with the new boundary condition therefore $c(s(t),t) = 0$. This boundary chemotaxes up the local conentration gradient according to the relation:

$$\partial_t s(t) = \frac{k}{c_0} \partial_x c(s(t),t), \tag{14}$$

where k is some yet-to-be-determined constant relating the gradient to the instantaneous speed of chemotaxis.

If we then consider the following solution to the heat equation:

$$c(x,t) = \frac{c_0}{\operatorname{erfc}\alpha}\left(\operatorname{erf}\frac{x}{\sqrt{4D_c t}} - \operatorname{erf}\alpha\right), \tag{15}$$

$$\partial_t c(x,t) = -\frac{c_0 x}{\operatorname{erfc}\alpha\sqrt{4\pi D_c t^3}}\exp\frac{-x^2}{4D_c t}, \tag{16}$$

$$\partial_x c(x,t) = \frac{c_0}{\operatorname{erfc}\alpha\sqrt{\pi D_c t}}\exp\frac{-x^2}{4D_c t}, \tag{17}$$

$$\partial_{xx} c(x,t) = -\frac{c_0 x}{\operatorname{erfc}\alpha\sqrt{4\pi D_c^3 t^3}}\exp\frac{-x^2}{4D_c t}, \tag{18}$$

As the boundary condition requires that $c(s(t),t) = 0$,

$$\operatorname{erf}\frac{s(t)}{\sqrt{4D_c t}} = \operatorname{erf}\alpha \tag{19}$$

$$s(t) = \alpha\sqrt{4D_c t} \tag{20}$$

$$\partial_t s(t) = \alpha\sqrt{\frac{D_c}{t}} \tag{21}$$

In general, the motion of the wave of cells in mazes is at constant speed, rather than following a $1/\sqrt{t}$ form. Nonetheless, we can compare the times taken to travel some distance L to provide approximate estimate of α in terms of cell speed v. Equating these times gives:

$$\frac{L}{v} = \frac{L^2}{4D_c\alpha^2} \tag{22}$$

$$\alpha = \sqrt{\frac{vL}{4D_c}}. \tag{23}$$

We can now define the gradient at the position of the cell wave degrading a semi-infinite region of chemoattractant in terms of measurable parameters, both for the case where the wave is stationary and where it is moving. We will now refer to the stationary case as $c_S(x,t)$ and the moving case as $c_M(x,t)$. For an arbitary gradient steepness k where $k > 0$, there is clearly some time t_S after which $\partial_x c_S(0,t_S) = k$. There is also a time t_M for which $\partial_x c_M(s(t_M),t_M) = k$. Using this, we can find t_S as a function of t_M as follows:

$$\partial_x c_S(0,t_S) = \partial_x c_M(s(t_M),t_M) \tag{24}$$

$$\frac{c_0}{\sqrt{4\pi D_c t_S}} = \frac{1}{\operatorname{erfc}\alpha}.\frac{c_0}{\sqrt{4\pi D_c t_M}}\exp(-s(t_M)^2/4D_c t_M) \tag{25}$$

$$\frac{1}{\sqrt{t_S}} = \frac{1}{\operatorname{erfc}\alpha}.\frac{1}{\sqrt{t_M}}\exp(-\alpha^2) \tag{26}$$

$$t_S = \gamma t_M \tag{27}$$

where $\gamma = \mathrm{e}^{2\alpha^2}\ \mathrm{erfc}^2\,\alpha$. A simple sense check shows that, for $v = 0$ we get $\alpha = 0$ and $\gamma = 1$, showing that, where the is no movement, we see no change in the time taken to reach a particular gradient steepness. For all $\alpha > 0$, $\gamma < 1$, meaning that the time taken to reach a particular gradient is longer when cells migrate, thereby confirming our initial intuition that such migration would sharpen the gradient.

This finding rests on the assumption that cells migrate in a semi-unbounded domain. In order to confirm the validity of this finding, and test its applicability to maze parts of finite length, we performed simulations of cells migrating up to, or sitting still at a decision point (See Fig. **S8**A). We varied the length of the dead end, and measured relative error for both the uncorrected solution, and the solution corrected by γ. The correction improved the accuracy of our analytical solution for moving cells for all dead-end lengths, with a residual error peaking at 10% of the simulated value, and improving as L increased. These differences are particularly low given that the simulations also have different degradation dynamics and simulate movement and diffusion within channels of some width.

1.4 Flux from a branching dead end

In trying to understand the chemotactic mirage discussed in the main text, we considered the possibility that maze shape could change the profile of attractant flux, and that this may be the key determinant of chemoattraction, rather than the absolute attractant quantity which is of course much higher in the attractant well. We consider the decision cells face as they approach a T junction, with an attractant well on one side and on the other a branching dead end of variable length. We found that the number of branches (and thus, the attractant flux to the junction) similarly influenced cell decisions. Numerical solutions to Eqs. 85 and 100 show that mirages are only apparent for number of branches $k > 1$. For distances to the true attractant well of 1mm, mirages require the the distance from the decision point to the branching point to be within $100\mu m$ (Fig. S9). For long live ends (3mm or more), which are still reasonable distances *in-vivo*, mirages can be much stronger, longer lived, and effective.

2 Assorted useful solutions to the heat equation

In this work, we are interested in the interaction between diffusible attractants or chemokines, a population of cells, and a structured, complex environment. In order to simplify our model from the full, coupled system of reaction, diffusion and advection driving it, we assume that advection is negligible and that our main reaction of importance can be described with the appropriate choice of boundary conditions. In all cases, we must still satisfy the diffusion equation for a molecule of diffusibility D_c:

$$\partial_t c(x,t) = D_c \partial_{xx} c(x,t). \tag{28}$$

The following sections describe some solutions that are useful for work on semi-1D diffusion problems, such as those we have explored.

2.1 Solution with Dirichlet boundary conditions

We desire a solution satisfying the fixed-concentration boundary conditions $c(0,t) = c_0,\ \ c(L,t) = c_L,\ \ c(x,0) = c_I$. We begin by finding the steady state of the system $c_S(x)$:

$$
\begin{aligned}
c(x,t) &\underset{t\to\infty}{\equiv} c_S(x) && (29)\\
\partial_t c_S(x) &= 0 \therefore \partial_{xx} c_S(x) = 0 && (30)\\
c_S(x) &= A_1 x + A_2 && (31)\\
c_S(0) &= c_0 \implies A_2 = c_0 && (32)\\
c_S(L) &= c_L \implies A_1 = \frac{c_1 - c_0}{L} && (33)\\
c_S(x) &= c_0 + \frac{c_L - c_0}{L} x && (34)
\end{aligned}
$$

As a linear combination of solutions must also be a solution, we can use this steady state to find a related homogeneous problem:

$$
\begin{aligned}
u(x,t) &= c(x,t) - c_S(x) \ \therefore\ u(0,t) = 0,\ u(L,t) = 0, && (35)\\
\partial_t u(x,t) &= \partial_t c(x,t) - \cancel{\partial_t c_S(x)}, && (36)\\
\partial_{xx} u(x,t) &= \partial_{xx} c(x,t) - \cancel{\partial_{xx} c_S(x)}, && (37)
\end{aligned}
$$

By separation of variables, with a separation constant $-\alpha^2$, we can reach the Fourier solution to the heat equation. As $u(0,t) = 0$, we reduce this to only the sine series:

$$
\begin{aligned}
u(x,t) &= \sum_{n=1}^{\infty} B_n \sin \alpha x \exp(-\alpha^2 D_c t), \quad u(L,t) = 0 \implies \alpha = \frac{n\pi}{L} && (38)\\
u(x,t) &= \sum_{n=1}^{\infty} B_n \sin \frac{n\pi x}{L} \exp\big(-n^2\pi^2 D_c t/L^2\big), && (39)\\
u(x,0) &= \sum_{n=1}^{\infty} B_n \sin \frac{n\pi x}{L}. && (40)
\end{aligned}
$$

Eq. 50 shows us that our B_n are simply the Fourier components of our initial condition. They can therefore be found directly from the initial condition $u(x,0)$:

$$
\begin{aligned}
u(x,0) &= \big(c_L - c_0\big)\bigg(1 - \frac{x}{L}\bigg), && (41)\\
B_n &= \frac{2(c_L - c_0)}{L}\int_0^L \bigg(1 - \frac{x}{L}\bigg)\sin\frac{n\pi x}{L}\,\mathrm{d}x && (42)\\
&= \frac{2(c_L - c_0)}{n\pi} && (43)\\
c(x,t) &= u(x,t) + c_S(x) && (44)\\
&= c_0 + \big(c_L - c_0\big)\frac{x}{L}\\
&+ \sum_{n=1}^{\infty}\frac{2}{n\pi}\big(c_I - c_0 + (-1)^{n+1}(c_I - c_L)\big)\sin\frac{n\pi x}{L}\exp\big(-n^2\pi^2 D_c t/L^2\big) && (45)
\end{aligned}
$$

In this work, we only use the case where $c_0 = 0$, as the lower boundary condition is held at this value by the migrating wave of cells, and $c_I = c_L$ as we fill each maze with an initially uniform attractant profile. We therefore make note of the final simplification:

$$
c(x,t) = \frac{c_L x}{L} + \sum_{n=1}^{\infty}\frac{2c_L}{n\pi}\sin\frac{n\pi x}{L}\mathrm{e}^{-n^2\pi^2 D_c t/L^2} \tag{46}
$$

2.2 Solution with mixed boundary conditions

Here we represent a dead end at $x = L$, such that we can apply a zero flux boundary condition there. As such, we have $c(0,t) = c_0,\ \ \partial_x c(L,t) = 0,\ \ c(x,0) = c_L$. The steady state is trivially a uniform profile of concentration c_0. We can therefore define the related homogeneous problem for $u(x,t) = c(x,t) - c_0$.

Similarly to the previous case, we can use separation of variables and the left-hand boundary

condition to arrive at the Fourier sine series solution:

$$
\begin{aligned}
u(x,t) &= \sum_{n=1}^{\infty} B_n \sin \alpha x \exp(-\alpha^2 D_c t), && (47)\\
\partial_x u(L,t) &= 0 \implies \alpha = (n-1/2)\pi/L && (48)\\
u(x,t) &= \sum_{n=1}^{\infty} B_n \sin \frac{(n-1/2)\pi x}{L} \exp\big(-(n-1/2)^2\pi^2 D_c t/L^2\big), && (49)\\
u(x,0) &= \sum_{n=1}^{\infty} B_n \sin \frac{(n-1/2)\pi x}{L}. && (50)\\
\therefore B_n &= \frac{2\big(c_L - c_0\big)}{L} \int_0^L \sin \frac{(n-1/2)\pi x}{L}\, \mathrm{d}x && (51)\\
&= \frac{4(c_L - c_0)}{(2n+1)\pi}, && (52)\\
u(x,t) &= \sum_{n=1}^{\infty} \frac{4(c_L - c_0)}{(2n-1)\pi} \sin \frac{(2n-1)\pi x}{2L} \mathrm{e}^{-(2n-1)^2\pi^2 D_c t/4L^2} && (53)\\
c(x,t) &= u(x,t) + c_0, && (54)\\
&= c_0 + \sum_{n=1}^{\infty} \frac{4(c_L - c_0)}{(2n-1)\pi} \sin \frac{(2n-1)\pi x}{2L} \mathrm{e}^{-(2n-1)^2\pi^2 D_c t/4L^2} && (55)
\end{aligned}
$$

Again, we are interested in the simplified case where, at the left-hand boundary, all attractant is depleted by the wave of migrating cells, and so $c_0 = 0$. This gives us our simplified case:

$$
c(x,t) = \sum_{n=1}^{\infty} \frac{4c_L}{(2n-1)\pi} \sin \frac{(2n-1)\pi x}{2L} \mathrm{e}^{-(2n-1)^2\pi^2 D_c t/4L^2} \tag{56}
$$

2.3 Solution with time-dependent Dirichlet boundary conditions

When considering the branches of mazes, it may be more useful to consider the arcs between them piecewise, with the junctions between them treated as time-dependent fixed-concentration boundaries, the precise nature of which we will determine later. Our boundaries, then, are $c(0,t) = f(t)$, $c(L,t) = g(t)$, $c(x,0) = c_L$, where for consistency we still use c_L to describe the initial, uniform concentration with which we flood all parts of the maze. We approach this using the method of eigenfunction expansions. We first consider a solution to the related homogeneous problem. The spatial component then gives us the eigenvalue problem:

$$
\partial_{xx}\Phi_n(x) + \alpha_n^2 \Phi_n = 0, \;\; \Phi_n(0) = 0, \;\; \Phi_n(L) = 0 \tag{57}
$$

We can define a simple function $s(x,t)$ that obeys the boundary conditions, such that for a function $u(x,t) = c(x,t) - s(x,t)$, the homogeneous boundary conditions apply. We then write $u(x,t)$ as

an expansion in terms of these spatial eigenfunctions as follows:

$$u(x,t) = c(x,t) - s(x,t), \implies u(0,t) = 0, \;\; u(L,t) = 0, \tag{58}$$

$$u(x,t) = \sum_{n=1}^{\infty} u_n(t)\Phi_n(x), \tag{59}$$

$$\partial_t u(x,t) = \sum_{n=1}^{\infty} \partial_t u_n(t)\Phi_n(x), \tag{60}$$

$$\partial_{xx} u(x,t) = \sum_{n=1}^{\infty} u_n(t)\partial_{xx}\Phi_n(x), \tag{61}$$

$$= \sum_{n=1}^{\infty} -\alpha_n^2 u_n(t)\Phi_n(x). \tag{62}$$

Here, we have assumed that term-by-term differentiation is allowable, and have used the eigenvalue equation to substitute out our $\partial_{xx}\Phi_n(x)$ terms, in order that both infinite series are expressed in terms of the unmodified spatial eigenfunctions. We can now return to our original problem by substituting $u(x,t)$ into the heat equation:

$$\partial_t c(x,t) = \partial_t u(x,t) + \partial_t s(x,t), \tag{63}$$

$$\partial_{xx} c(x,t) = \partial_{xx} u(x,t) + \partial_{xx} s(x,t) \therefore \tag{64}$$

$$\partial_t s(x,t) + \sum_{n=1}^{\infty} \partial_t u_n(t)\Phi_n(x) = D_c\left(\partial_{xx} s(x,t) - \sum_{n=1}^{\infty} \alpha_n^2 u_n(t)\Phi_n(x)\right), \tag{65}$$

$$\sum_{n=1}^{\infty} \left(\partial_t u_n(t) + D_c\alpha_n^2 u_n(t)\right)\Phi_n(x) = Q(x,t), \tag{66}$$

$$\text{where} \;\; Q(x,t) = D_c\partial_{xx} s(x,t) - \partial_t s(x,t) \tag{67}$$

As we express the LHS entirely in terms of our spatial eigenfunctions $\Phi_n(x)$, we now seek to express $Q(x,t)$ in terms of the same,

$$Q(x,t) = \sum_{n=1}^{\infty} q_n(t)\Phi(x) \therefore \tag{68}$$

$$\sum_{n=1}^{\infty} \left(\partial_t u_n(t) + D_c\alpha_n^2 u_n(t)\right)\Phi_n(x) = \sum_{n=1}^{\infty} q_n(t)\Phi(x). \tag{69}$$

It is very important to note that at this stage we have imposed on $Q(x,t)$ a series of spatial eigenfunctions chosen for meeting the homogeneous boundary conditions of $u(x,t)$, even though $Q(x,t)$ almost certainly does not obey these conditions. The solution we construct therefore applies to the region excluding the boundaries, *i.e.* $x \in (0,L)$ but not $x \in [0,L]$.

As these eigenfunctions are orthogonal, this equation holds for each harmonic (*i.e.* each n) separately, giving us:

$$\partial_t u_n(t) + D_c\alpha_n^2 u_n(t) = q_n(t) \tag{70}$$

where we can sift out the $q_n(t)$ by using the orthogonality of the eigenfunctions:

$$q_n(t) = \frac{\int_0^L Q(x,t)\Phi_n(x)\,\mathrm{d}x}{\int_0^L \Phi_n^2(x)\,\mathrm{d}x}. \tag{71}$$

This reduces the problem to the solution of a first-order ODE for the $u_n(t)$.

We must now begin to consider the specifics of our case. In order to achieve the homogeneous boundary conditions required for $u(x,t)$, we will have:

$$\begin{aligned} s(x,t) &= f(t) + \frac{x}{L}\big(g(t) - f(t)\big), & (72)\\ \partial_t s(x,t) &= \partial_t f(t) + \frac{x}{L}\big(\partial_t g(t) - \partial_t f(t)\big), & (73)\\ \partial_{xx} s(x,t) &= 0, & (74) \end{aligned}$$

Solution of the original eigenvalue problem for $u(x,t)$ gives us $\Phi_n(x) = \sin(\alpha x)$ and $\alpha = n\pi/L$. Eq. 71 therefore reduces to the expression for the coefficients of a Fourier sine series:

$$\begin{aligned} \int_0^L \sin^2 \frac{n\pi x}{L}(x)\,\mathrm{d}x = L/2 \;\therefore & & (75)\\ q_n &= \frac{2}{L}\int_0^L Q(x,t)\sin\frac{n\pi x}{L}\,\mathrm{d}x, & (76)\\ &= \frac{-2}{L}\int_0^L \partial_t s(x,t)\sin\frac{n\pi x}{L}\,\mathrm{d}x, & (77)\\ &= \frac{-2\partial_t f(t)}{L}\int_0^L \sin\frac{n\pi x}{L}\,\mathrm{d}x - \frac{-2\big(\partial_t g(t) - \partial_t f(t)\big)}{L^2}\int_0^L x\sin\frac{n\pi x}{L}\,\mathrm{d}x, & (78)\\ &= \frac{2}{n\pi}\Big[(-1)^n\partial_t g(t) - \partial_t f(t)\Big]. & (79) \end{aligned}$$

Inserting this into Eq. 70 and multiplying through by the integrating factor $\mathrm{e}^{\alpha_n^2 D_c t}$ gives

$$\begin{aligned} \mathrm{e}^{\alpha_n^2 D_c t}\frac{\mathrm{d}u_n(t)}{\mathrm{d}t} + \mathrm{e}^{\alpha_n^2 D_c t} D_c \alpha_n^2 u_n(t) &= \mathrm{e}^{\alpha_n^2 D_c t}\frac{2}{n\pi}\frac{\mathrm{d}}{\mathrm{d}t}\Big[(-1)^n g(t) - f(t)\Big] & (80)\\ \frac{\mathrm{d}}{\mathrm{d}t}\Big(\mathrm{e}^{\alpha_n^2 D_c t}u_n(t)\Big) &= \mathrm{e}^{\alpha_n^2 D_c t}\frac{2}{n\pi}\frac{\mathrm{d}}{\mathrm{d}t}\Big[(-1)^n g(t) - f(t)\Big] \;\therefore & (81)\\ \int_0^t \partial_\tau\Big(\mathrm{e}^{\alpha_n^2 D_c \tau}u_n(\tau)\Big)\,\mathrm{d}\tau &= \int_0^t \frac{2\mathrm{e}^{\alpha_n^2 D_c \tau}}{n\pi}\frac{\mathrm{d}}{\mathrm{d}\tau}\Big[(-1)^n g(\tau) - f(\tau)\Big]\,\mathrm{d}\tau & (82)\\ \mathrm{e}^{\alpha_n^2 D_c t}u_n(t) - u_n(0) &= \frac{2}{n\pi}\int_0^t \mathrm{e}^{\alpha_n^2 D_c \tau}\frac{\mathrm{d}}{\mathrm{d}\tau}\Big[(-1)^n g(\tau) - f(\tau)\Big]\,\mathrm{d}\tau. & (83) \end{aligned}$$

The $u_n(0)$ are the Fourier components of $u(x,0) = c(x,0) - s(x,0)$, but at $t = 0$ all values of concentration are uniformly c_L, giving $u(x,0) = 0$. Thus, these coefficients all evaluate to zero,

leaving

$$u_n(t) = \frac{\frac{2}{n\pi}\int_0^t \mathrm{e}^{\alpha_n^2 D_c \tau}\frac{\mathrm{d}}{\mathrm{d}\tau}\Big[(-1)^n g(\tau) - f(\tau)\Big]\,\mathrm{d}\tau}{\mathrm{e}^{\alpha_n^2 D_c t}}, \tag{84}$$

which can be determined once the boundary condition functions are known. Our expression for $c(x,t)$ is, then,

$$c(x,t) = \sum_{n=1}^{\infty} u_n(t)\sin\frac{n\pi x}{L} + f(t) + \frac{x}{L}\Big(g(t) - f(t)\Big) \tag{85}$$

As a basic test of the validity of this solution (and therefore, of the assumption made), we will test its ability to recapitulate a small section of a known function. We will take the Dirichlet solution with static boundary conditions as our test case, and see if we can recreate the section for $x \in (L/4,\ 3L/4)$ using our solution with time-dependent boundaries.

$$\begin{aligned}
f(t) &= \frac{c_L}{4} + \sum_{m=1}^{\infty}\frac{2c_L}{m\pi}\sin\frac{m\pi}{4}\mathrm{e}^{-m^2\pi^2 D_c t/4L^2}, && (86)\\
\partial_t f t &= -\frac{D_c c_L}{2L^2}\sum_{m=1}^{\infty} m\pi\sin\frac{m\pi}{4}\mathrm{e}^{-m^2\pi^2 D_c t/4L^2} && (87)\\
g(t) &= \frac{3c_L}{4} + \sum_{m=1}^{\infty}\frac{2c_L}{m\pi}\sin\frac{3m\pi}{4}\mathrm{e}^{-m^2\pi^2 D_c t/4L^2}, && (88)\\
\partial_t g t &= -\frac{D_c c_L}{2L^2}\sum_{m=1}^{\infty} m\pi\sin\frac{3m\pi}{4}\mathrm{e}^{-m^2\pi^2 D_c t/4L^2}. && (89)
\end{aligned}$$

Inserting these into Eq. 84 and evaluating the integral gives

$$\begin{aligned}
u_n(t) &= \frac{4c_L}{\pi^2}\sum_{n=1}^{\infty}\frac{m}{n}\frac{1}{4n^2-m^2}\left[(-1)^{n+1}\sin\frac{3m\pi}{4} + \sin\frac{m\pi}{4}\right]\\
&\quad .\quad \left[\exp\big(-m^2\pi^2 D_c t/4L^2\big) - \exp\big(-4n^2\pi^2 D_c t/4L^2\big)\right] && (90)
\end{aligned}$$

Substituting these $u_n(t)$ into Eq. 85 recapitulates exactly the expected solution within the specified domain (Fig. **S10**).

2.4 Solution with mixed time dependent boundary conditions

Much of our argument in this case is shared with the previous section. We are instead applying the boundaries $c(0,t) = f(t),\ \partial_x c(L,t) = h(t),\ c(x,0) = c_L$. The general argument up to Eqs. (70, 71) still applies. We instead choose $s(x,t)$ to satisfy these boundary conditions:

$$
\begin{aligned}
s(x,t) &= f(t) + xh(t), && (91)\\
\partial_t s(x,t) &= \partial_t f(t) + x\partial_t h(t), && (92)\\
\partial_{xx} s(x,t) &= 0 && (93)
\end{aligned}
$$

Following the logic of our previous example, we must now find the q_n using our eigenfuctions $\sin \alpha x$, however here $\alpha_n = (n - 1/2)\pi/L$.

$$
\begin{aligned}
\int_0^L \sin^2 \alpha_n x \, \mathrm{d}x = L/2 \ \therefore && (94)\\
q_n &= \frac{2}{L}\int_0^L Q(x,t)\sin\alpha_n x \, \mathrm{d}x, && (95)\\
&= -\frac{2\partial_t f(t)}{L}\int_0^L \sin\alpha_n x \, \mathrm{d}x - \frac{2\partial_t h(t)}{L}\int_0^L x\sin\alpha_n x \, \mathrm{d}x, && (96)\\
&= \frac{-4}{(2n-1)\pi}\frac{\mathrm{d}}{\mathrm{d}t}\left[f(t) + \frac{2L}{\pi}\frac{(-1)^{n+1}}{(2n-1)}h(t)\right], \ \therefore && (97)\\
u_n(t) &= \frac{-\frac{4}{(2n-1)\pi}\left[\frac{2L}{\pi}\frac{(-1)^{n+1}}{2n-1}\left(h_n(0) + \int_0^t \mathrm{e}^{\alpha_n^2 D_c \tau}\frac{\mathrm{d}h(\tau)}{\mathrm{d}\tau}\,\mathrm{d}\tau\right) + \int_0^t \mathrm{e}^{\alpha_n^2 D_c\tau}\frac{\mathrm{d}f(\tau)}{\mathrm{d}\tau}\,\mathrm{d}\tau\right]}{\mathrm{e}^{\alpha_n^2 D_c t}} && (98)
\end{aligned}
$$

with the final step evaluating $u_n(0)$ using the initial conditions. Four our study, we are cheifly interested in the case where $h(t) = 0$, representing the no-flux condition of dead ends. This gives us the somewhat cleaner:

$$
u_n(t) = -\frac{4\mathrm{e}^{-\alpha_n^2 D_c t}}{(2n-1)\pi}\int_0^t \mathrm{e}^{\alpha^2 D_c \tau}\frac{\mathrm{d}f(\tau)}{\mathrm{d}\tau}\,\mathrm{d}\tau \tag{99}
$$

Once the form for the boundary conditions is known, we have all we need to calculate c:

$$
c(x,t) = f(t) + xh(t) + \sum_{n=1}^{\infty} u_n(t)\sin\frac{(n-1/2)\pi x}{L}. \tag{100}
$$

We can test the ability of this form to correctly predict the latter half of the solution for static mixed boundary conditions. Here, $h(t) = 0$, $c(x,0) = c_L$:

$$
\begin{aligned}
f(t) &= \frac{4C_L}{\pi}\sum_{m=1}^{\infty}\frac{\sin\frac{(2m-1)\pi}{4}}{2m-1}\exp\big(-(2m-1)^2\pi^2 D_c t/16L^2\big), && (101)\\
u_n(t) &= \frac{16c_L}{\pi^2}\sum_{m=1}^{\infty}\frac{2m-1}{2n-1}\frac{\sin\big((2m-1)\pi/4\big)}{4(2n-1)^2-(2m-1)^2}\\
&\quad \cdot \left[\exp\left(-\frac{(2m-1)^2\pi^2 D_c t}{16L^2}\right) - \exp\left(-4\frac{(2n-1)^2\pi^2 D_c t}{16L^2}\right)\right]. && (102)
\end{aligned}
$$

As can be seen in Fig. **S10**, these $u_n(t)$ recapitulate the region of the target solution precisely.

Supplementary figures

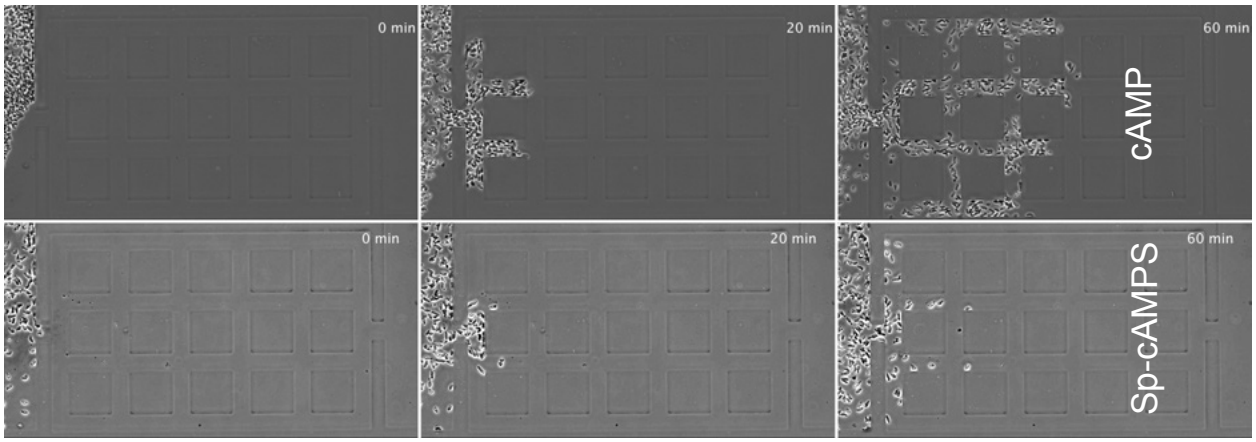

Figure S1: **Progress into mazes relies on attractant breakdown.** Progress in a similar maze at 0, 20 and 60 minutes for a self-generated cAMP gradient vs a linear gradient of non-degradable Sp-cAMPS. Poor progress toward Sp-cAMPS confirms that attractant degradation is the driver of our other observations.

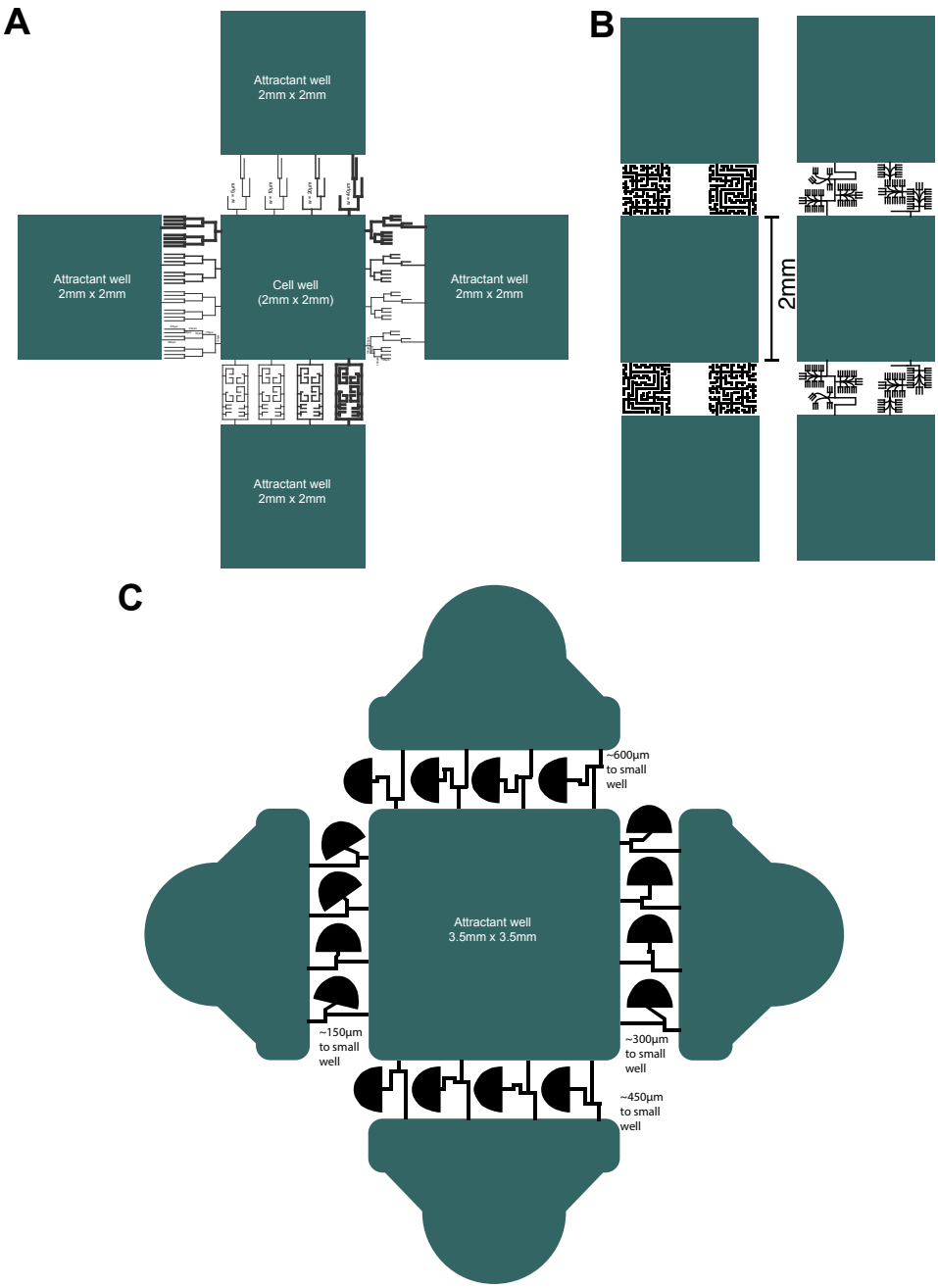

Figure S2: **Maze designs used in this study. A)** The long, short and simple mazes are shown to the left, right and top respectively. The maze design toward the bottom is not used in this study. **B)** Designs for easy and hard mazes. **C)** Design for the mirage maze device used in Fig. 5.

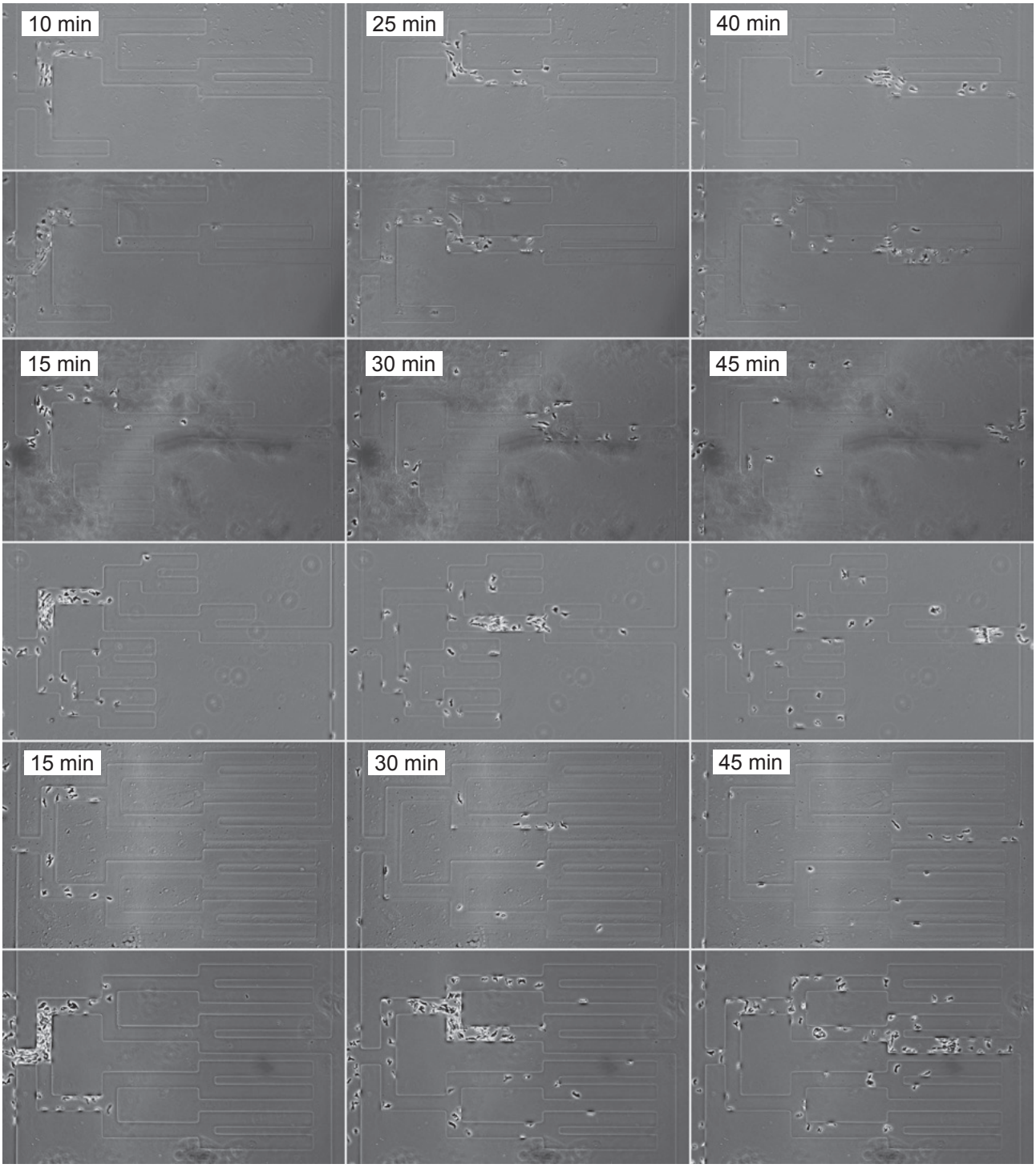

Figure S3: **Montages of experimental repeats.** Two additional examples of *D. discoideum* solving each maze design from main text Fig. 2 are shown.

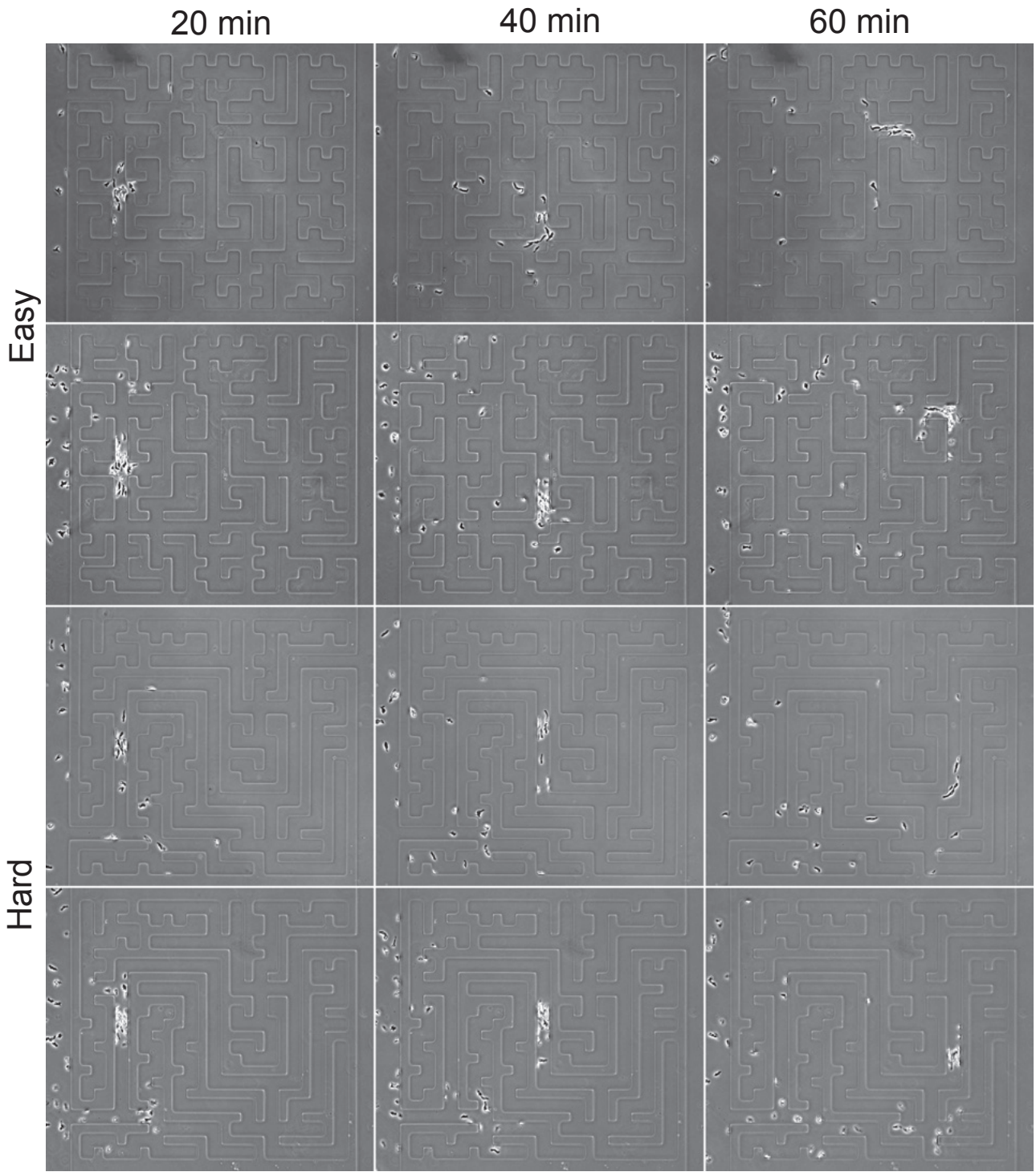

Figure S4: **Experimental repeats of labyrinth mazes.** Two additional examples of *D. discoideum* solving each labyrinth design from main text Fig. 6.

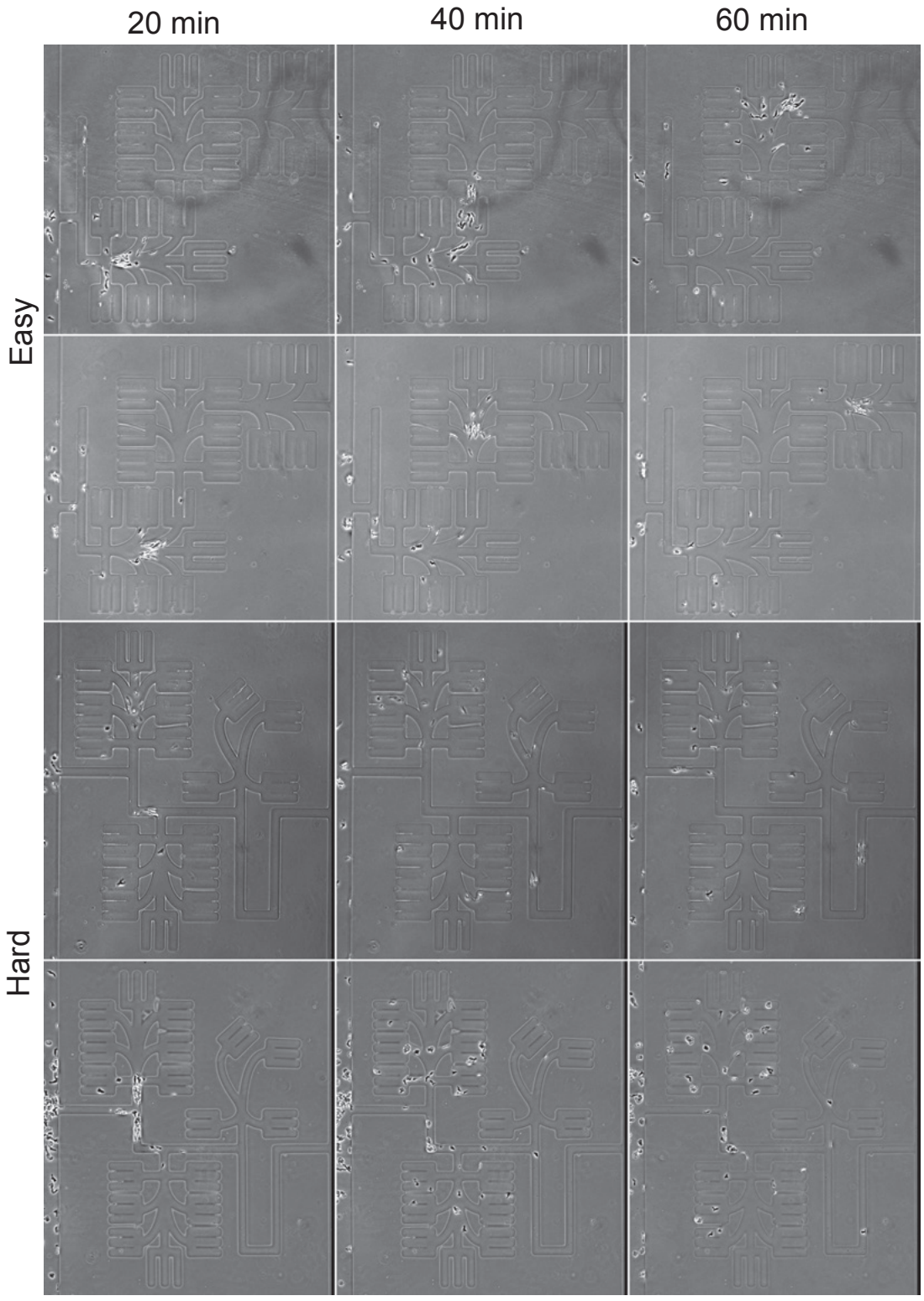

Figure S5: **Experimental repeats of trident mazes.** Two additional examples of *D. discoideum* solving each Trident design from main text Fig. 6.

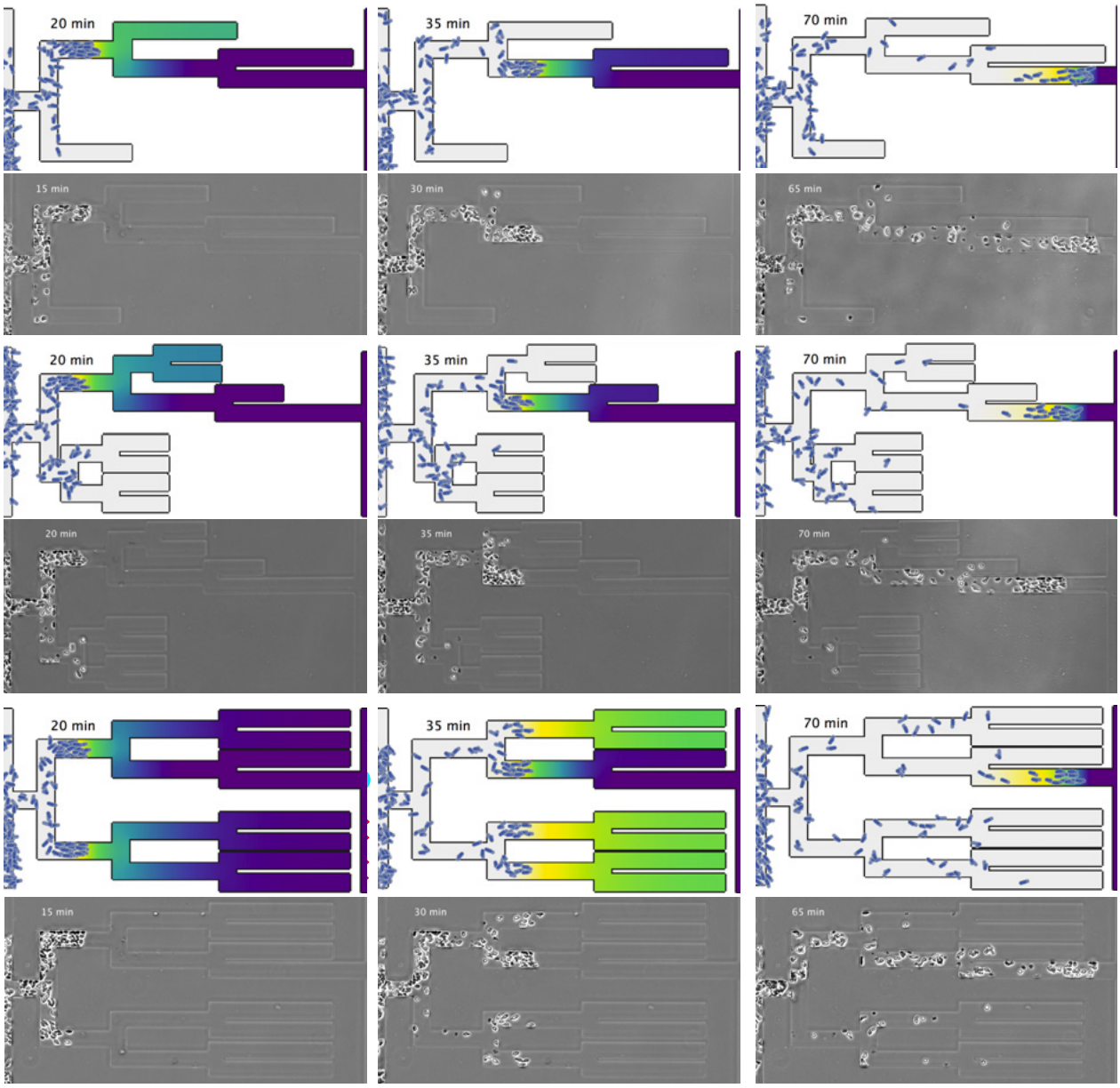

Figure S6: **Montages of experiments in NC4 parental strain.** Experiments and paired simulations in the parental strain of the cells used in main text Fig. 2. Behaviour is similar to that of the *aca-* cells. Though caffeine is used to block cAMP secretion, in the confined space of the maze some streaming is still evident.

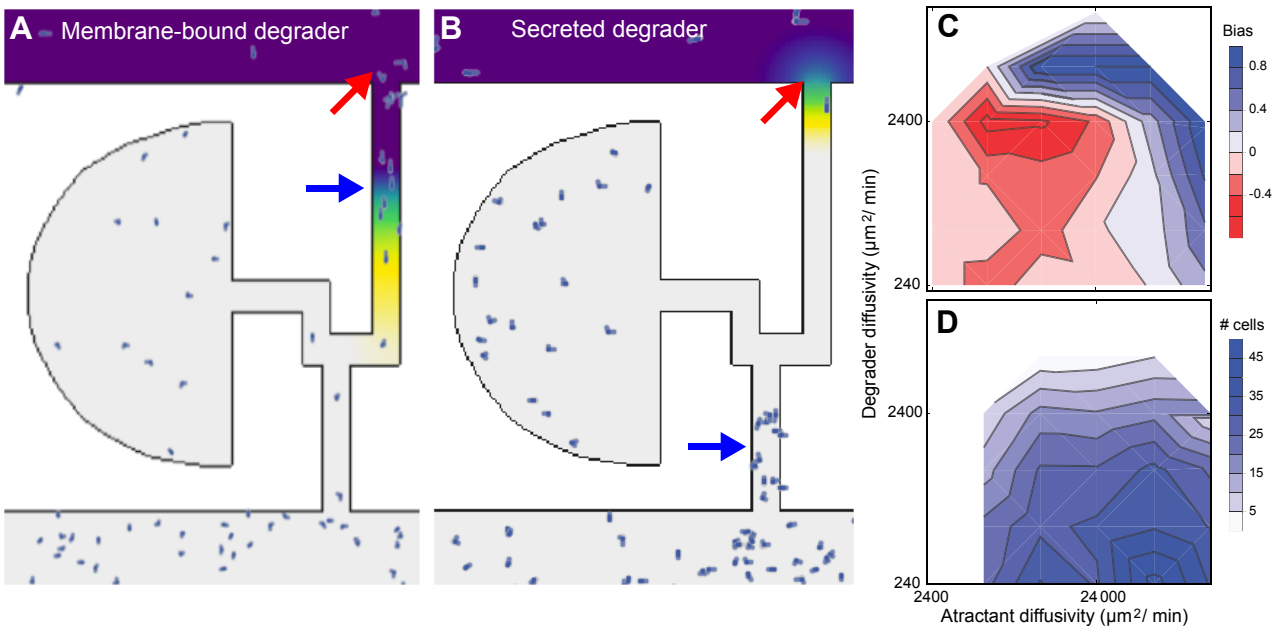

Figure S7: **Changes to maze dynamics when degrading enzyme is secreted. (A,B)** Examples of mazes with membrane-bound degrader and a secreted degrading molecule (SDM). When degradation is SDM dominated, attractant does not re-enter a maze after the initial wave of cells disperses, and attractant even becomes slightly depleted in the large reservoir (red arrows). This prevents the late recruitment of cells lost further down the maze that we observe both in the simulations of a membrane bound degrader (blue arrows) and in the matching experiments (Movie S5). **(C)** Bias scores for varying attractant and SDM diffusivities. Increasing the diffusivity of either moves the simulaion out of the experimentally verified negative bias region, with cells instead steering towards the large attractant reservoir. **(D)** A key difference between increasing attractant and SDM diffusivity is the total number of cells recruited to the maze. While high attractant diffusivity generally causes more cells to be recruited, high degrader diffusivity consistently causes fewer to be.

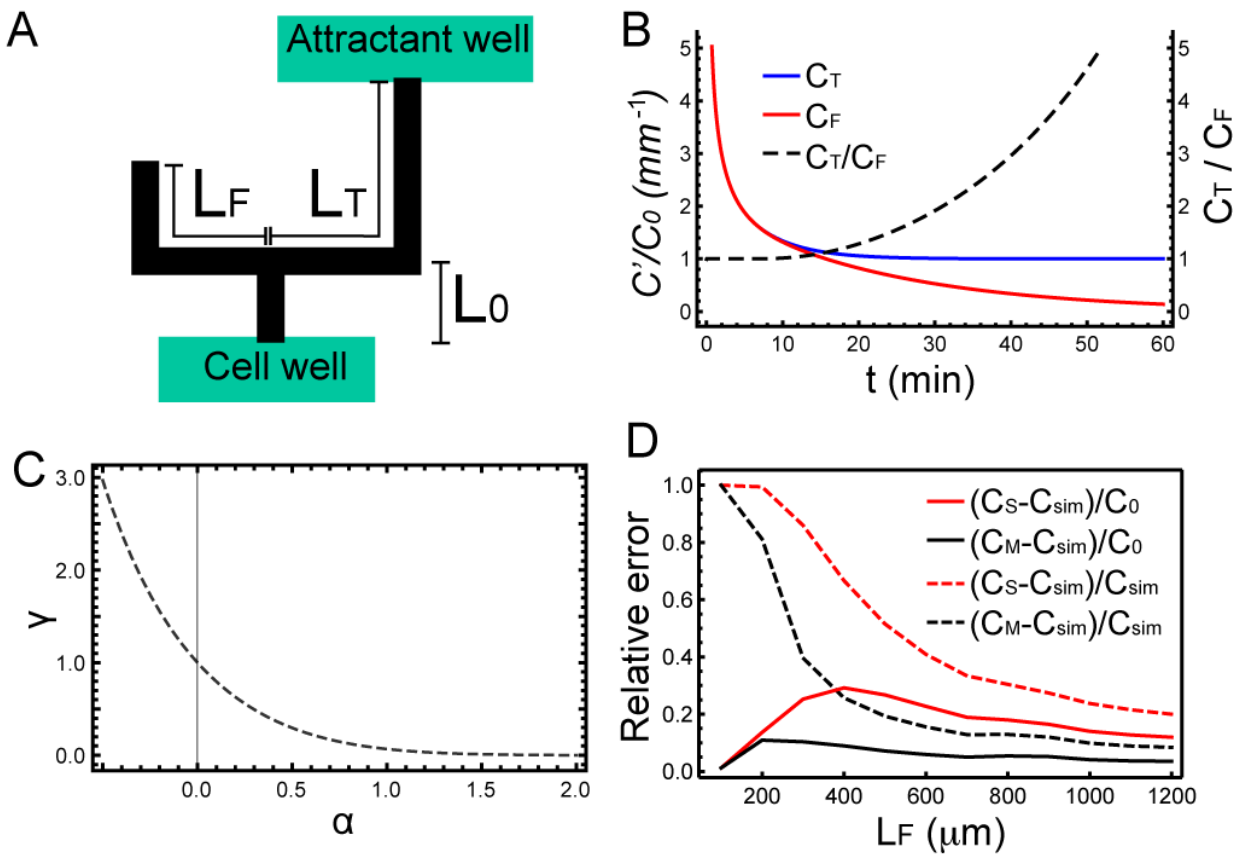

Figure S8: **Analytical prediction for decisions in a simple maze. A)** Diagram of the maze under consideration, consisting of an entrance channel of length L_0, a dead end of length L_F, and a channel connecting to the attractant well of length L_T. **B)** Gradient steepness at the decision point $x = 0$ for the true channel (blue), the false channel (red), and the ratio of these values (black, dashed).

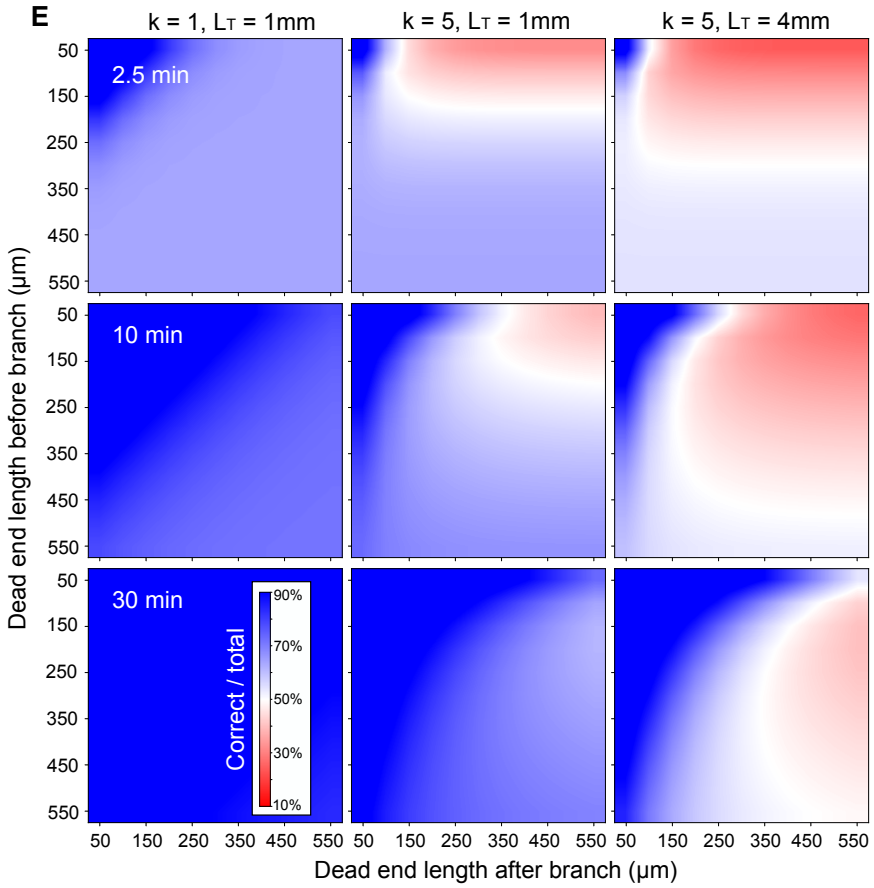

Figure S9: **Chemotactic mirages depend strongly on distance to the true attractant well.** Correct vs incorrect decisions are shown for various dead-end topologies. When k=1 and the dead end is unbranching, decisions are always better than 50-50 and improve over time. When the live end is around 1mm away, chemotactic mirages appear briefly, as long as the dead end branches within $100\mu m$ of the junction at which the cells make their decision. For long live ends (4mm shown here), chemotactic mirages can be strong and long-lasting.

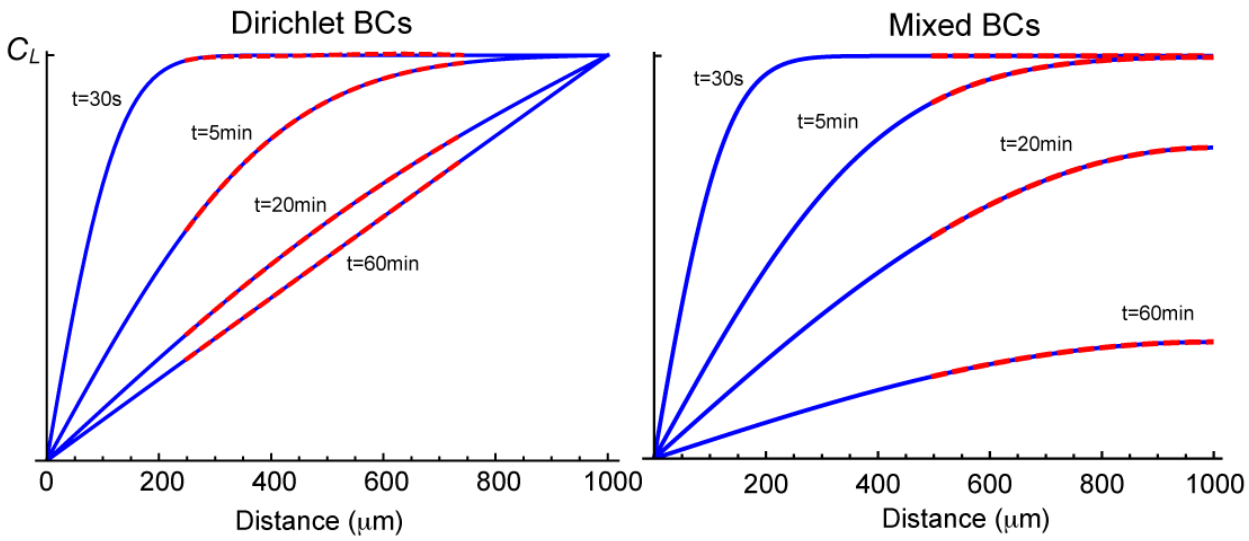

Figure S10: **Various analytical solutions to the heat equation.** **L** Solution for static (blue) and time-dependent (red) Dirichlet boundaries, using realistic diffusion parameters. **L** Solution for static (blue) and time-dependent (red) mixed boundaries, using realistic diffusion parameters.

Captions for supplementary movies

Movie S1. Self-generated gradients overcome the range limitation of passive gradient chemotaxis. Top to bottom: 1. Simulation of passive gradient response. 2. Simulation of self-generated gradient response. 3. *D. discoideum* chemotax to a passive gradient of Sp-cAMPS. 4. *D. discoideum* chemotax to initially uniform cAMP. Movies correspond to simulations and experiments in main text Fig. 1.

Movie S2. Simulations of maze solving via self-generated gradients. The three movies correspond to the simulation panels in main text Fig. 2.

Movie S3. Maze solving by *D. discoideum*. Mazes are initially filled uniformly with attractant. Movies correspond to experiments shown in main text Fig. 2.

Movie S4. Maze solving by cancer cells. Movies correspond to experiments shown in main text Fig. 2.

Movie S5. Dynamics of chemotactic migrages. Simulations are shown first, then corresponding experiments. In the left panel the majority of cells move into the small trap reservoir, rather than steering toward the large reservoir. In the middle panel this is also the case, but many cells rectify this decision, showing that the mirage does cease. In the right panel, the majority of cells steer towards the large reservoir.

Movie S6. Navigation of easy and hard labyrinths. Cells navigating the easy and hard labyrinth designs shown in main text Fig. 6. Simulations are shown first, then corresponding experiments.

Movie S7. Navigation of easy and hard trident mazes. Cells navigating the easy and hard trident designs shown in main text Fig. 6. Simulations are shown first, then corresponding experiments.